

# Data Comparisons and Summary of the Second Aeroelastic Prediction Workshop

Jennifer Heeg,<sup>\*</sup> Carol D. Wieseman,<sup>†</sup> and Pawel Chwalowski<sup>‡</sup>

*NASA Langley Research Center, Hampton, VA 23681-2199*

This paper presents the computational results generated by participating teams of the second Aeroelastic Prediction Workshop and compare them with experimental data. Aeroelastic and rigid configurations of the Benchmark Supercritical Wing (BSCW) wind tunnel model served as the focus for the workshop. The comparison data sets include unforced (“steady”) system responses, forced pitch oscillations and coupled fluid-structure responses. Integrated coefficients, frequency response functions, and flutter onset conditions are compared. The flow conditions studied were in the transonic range, including both attached and separated flow conditions. Some of the technical discussions that took place at the workshop are summarized.

## Nomenclature

### Roman Symbols

$C_p$	Coefficient of pressure
$f, f^*$	frequency, system’s primary frequency - Hz
M	Mach number
q	Dynamic pressure
$q_E$	Dynamic pressure at flutter onset, as determined by experiment
$q_F$	Dynamic pressure at flutter onset, as determined by simulation

### Greek Symbols

$\alpha$	Angle of attack
$\theta$	angular pitch displacement

### Acronyms

AePW	Aeroelastic Prediction Workshop
BSCW	Benchmark Supercritical Wing
CSD	Cross Spectral Density
DDES	Delayed Detached Eddy Simulation
DFT	Discrete Fourier Transform
FRF	Frequency Response Function
OTT	Oscillating Turntable
PAPA	Pitch And Plunge Apparatus
PSD	Power Spectral Density

---

<sup>\*</sup>Senior Research Engineer, Aeroelasticity Branch, MS 340, Senior Member AIAA.

<sup>†</sup>Senior Research Engineer, Aeroelasticity Branch, MS 340, Associate Fellow AIAA.

<sup>‡</sup>Senior Aerospace Engineer, Aeroelasticity Branch, MS 340, Senior Member AIAA.

## I. Introduction

Generations of aeroelasticians have worked to understand the physics of flutter and to develop methods of predicting the conditions under which flutter occurs. The high cost of getting it wrong and the complexity of the physics that we are trying to predict drive us to evaluate the validity of our tools and to establish the influences of choices we make in setting up an analysis.

The fundamental technical challenge of computational aeroelasticity (CAe) is to accurately predict the coupled behavior of the unsteady aerodynamic loads and the flexible structure. The objective in conducting workshops on aeroelastic prediction is to assess state of the art and state of the practice in computational aeroelasticity methods as practical tools for the prediction of static and dynamic aeroelastic phenomena. No comprehensive aeroelastic benchmarking validation standard currently exists, greatly hindering validation objectives. The aeroelastic prediction workshop series is intended to provide an open forum, to encourage transparent discussion of results and processes, to promote best practices and collaborations, and to develop analysis guidelines and lessons learned.

Numerous organizations have developed analytical methods and codes, each conducting their own validation effort. The current workshop series approaches the problem with multi-analyst code-to-code comparisons to assess the state of the art in computational aeroelasticity. The first Aeroelastic Prediction Workshop (AePW-1) was held in April 2012<sup>1-15</sup> and served as a first step in assessing the state of the art of computational methods for predicting unsteady flow fields and aeroelastic response. The second Aeroelastic Prediction Workshop (AePW-2), held in January 2016, built on the experiences of the first workshop, extending the benchmarking effort to aeroelastic flutter solutions. Technical and organizational information for the second Aeroelastic Prediction Workshop (AePW-2) was presented by Heeg et al.,<sup>16</sup> along with relevant lessons learned from AePW-1. The second AePW builds on those experiences.

The origins of the Aeroelastic Prediction Workshop series lie in 2009, based on the success of two other workshop series that have been conducted over the past decade: the Drag Prediction Workshop (DPW)<sup>17</sup> series and the High Lift Prediction Workshop (HiLiftPW)<sup>18</sup> series. At the outset, the AePW differed from the other workshops by focusing on unsteady flow characterization and on coupled fluid-structure solutions. Time has progressed, and the objectives of the DPW series have expanded to consider small static aeroelastic effects. The HiLiftPW objectives and methods have expanded to include some unsteady flow considerations, both in measurements and in computations.<sup>19</sup>

For code validations in general, the type of aerodynamic and/or aeroelastic phenomena to be analyzed is important since a validation process typically progresses from simpler to more challenging cases. For the AePW series, the approach taken is to utilize existing experimental data sets in a building-block approach to incrementally validate targeted aspects of CAe tools. The challenge selected for the first AePW was the accurate prediction of unsteady aerodynamic phenomena on essentially rigid, geometrically simple models, with an additional foray into systems with weak coupling between the fluid and the structure. Results from this first workshop helped guide the direction of the second workshop, with analyses extending to include flutter prediction and therefore, increasingly complicated flow fields.

The main focus of this paper is presentation of the combined computational aeroelastic results generated by the workshop participants for the BSCW configuration and comparing those results to the experimental data. Details associated with the BSCW geometry and test cases are presented first. The database comparisons for each test case are then presented.

Two of the lessons learned from AePW-1 were to focus the workshop on a single configuration, and have a benchmark case that is thought to be sufficiently predictable with all computational tools to be applied in the study. Both of these lessons were incorporated by the organizing committee in formulating the second workshop.

## II. Wind Tunnel Model and Testing

The single configuration chosen for analysis in AePW-2 was the Benchmark Supercritical Wing (BSCW). This configuration was analyzed for AePW-1 and drew the most post-workshop interest from the participating analysis teams. It was also the most poorly predicted case from the first workshop. A working group continued to analyze the experimental data and perform computations to better understand the physics governing the problem and the requirements on the computational tools to capture these physics.

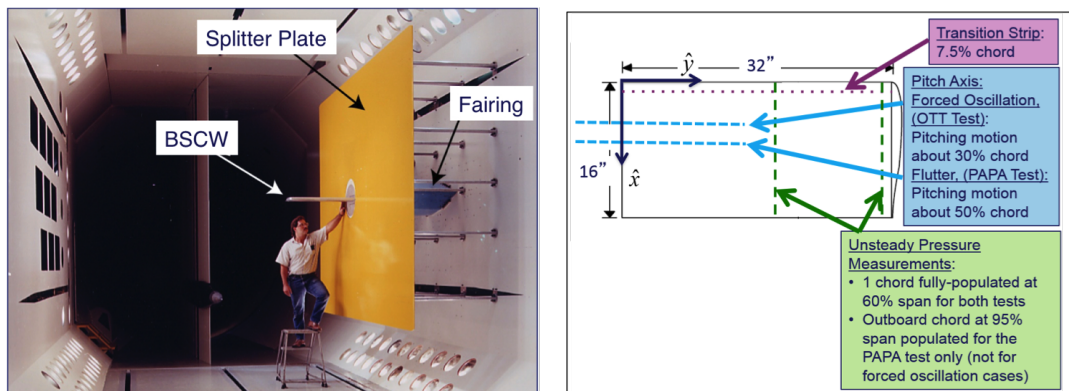
The BSCW model, shown in Figure 1, has a simple, rectangular, 16- x 32-inch wing planform, with a NASA SC(2)-0414 airfoil. The BSCW geometric reference parameters are shown in Table 1. The model was mounted to a large splitter plate, sufficiently offset from the wind-tunnel wall (40 inches) to (1) place the wing closer to the tunnel centerline and (2) be outside the tunnel wall boundary layer.<sup>20</sup> The wing was designed to be rigid, with all significant flexibility originating from the mounting structure. For instrumentation, the model has pressure ports at two chordwise

rows at the 60% and 95% span locations, with 22 ports on the upper surface, 17 ports on the lower surface, and 1 port at the leading edge for each row.

The BSCW model was tested in the NASA Transonic Dynamics Tunnel (TDT) in two test entries. Differences between the two tests and their associated data sets are provided in Table 2. The first BSCW test in the early 1990's, was performed on a flexible mount system, called the pitch and plunge apparatus (PAPA), which provides two-degree-of-freedom low-frequency flexible modes that emulate a plunge mode and a pitch mode. The BSCW/PAPA data consists of unsteady data at flutter points and averaged data on a rigidified apparatus at the flutter conditions. For this PAPA test, both the inboard row at the 60% span station and the outboard row at the 95% span station were populated with unsteady in-situ pressure transducers. The more recent test in 2000, which served as the basis for one of the AePW-1 test cases, was performed on the oscillating turntable (OTT), which provided forced pitch oscillation data. For this OTT test, however, only the inboard row at the 60% span station was populated with unsteady in-situ pressure transducers.

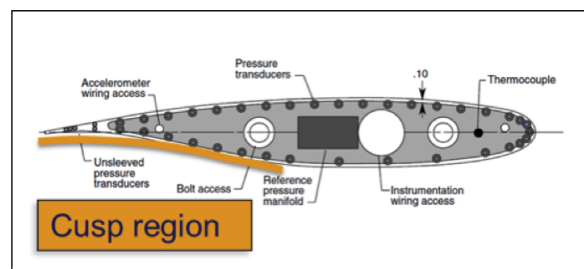
Both of the TDT tests were conducted with the sidewall slots open. The BSCW/PAPA test was conducted with several flow transition strip configurations, but only data using size #35 grit was used for the workshop comparisons. For the BSCW/OTT test, the boundary-layer transition was also fixed at 7.5% chord using size #30 grit.

Comparison with experimental data is a critical aspect in conducting a validation study. The quality and breadth of the data set are key components in assessing the goodness of the computations. The data sets used in the current effort lack many of the detailed measurements that are necessary for a thorough validation effort. The data sets contain what was thought necessary for aeroelastic code validation circa 1990. A further detrimental comment regarding the data set is that the original measurements are no longer available; only the reduced data that was published is available.



(a) Photograph of the BSCW model mounted on the OTT in the TDT.

(b) BSCW geometry.



(c) Cross-sectional view of the SC(2)-0414 airfoil, with BSCW instrumentation.

**Figure 1. BSCW Model.**

### III. Workshop Analysis Cases

The BSCW flow conditions used in AePW-1 were challenging. One of the technical outcomes of the effort that progressed between the workshops was a better understanding of the flow field physics. The detailed examination of the experimental data led to the assessment that shock-induced separated flow dominated the upper surface and the aft portion of the lower surface at the Mach 0.85 and  $5^\circ$  angle-of-attack case. To identify simpler analysis cases, the

**Table 1. BSCW Geometric Reference Parameters.**

Description	Symbol	Value
Reference chord	$c_{ref}$	16 inches
Model span	$b$	32 inches
Area	$A$	512 inch <sup>2</sup>
Moment reference point relative to axis system def.	$x_{ref}$	4.8 inches, 30%
	$y_{ref}$	0.0 inches
	$z_{ref}$	0.0 inches
Frequency Response Function reference quantity	FRF	Pitch angle

**Table 2. Differences between the Two BSCW TDT Test Configurations and Associated Data Sets.**

Test number	470 (year 1991)	548 (year 2000)
Mount system	PAPA	OTT
Pitch axis, % chord	50%	30%
Test medium	R-12	R-134a
Pressure transducer spanwise locations	60%, 95%	60%
Steady data configuration	Rigidized mount system	Unforced system
Forced oscillation data?	No	Yes
Flutter data?	Yes	No
Time history records?	No	Yes

entire set of available experimental data from the OTT test was assessed for separated flow using an isentropic flow relationship and rules of thumb.<sup>21</sup>

Simplifying the physics to a case that could be predicted by most methods, including linear methods, was the objective in choosing the primary analysis cases for AePW-2. Using the experimental information as a guide, two test cases just outside of the separated flow regime were emphasized for AePW-2 and are listed in Table 3. Steady and forced oscillation analyses were conducted at Mach 0.7, 3° angle of attack, and flutter analyses were conducted at Mach 0.74, 0° angle of attack. An optional case, Case 3 at Mach 0.85, 5° angle of attack, which was the re-analysis of the AePW-1 case, was encouraged to apply the higher fidelity tools. This optional case was divided into three subcases based on the source of dynamic excitation.

An important point to note is that experimental data is not available for all dynamic cases. In particular there is no experimental flutter data available for Case 3. A second important point is that not all cases require aeroelastically coupled simulations. Unforced system cases— sometimes termed steady— were treated as acting on rigid wings, although separate comparisons were made to static aeroelastic results when provided by the analysis teams. These rigid unforced system analyses are logical steps that are generally performed as starting points for coupled flexible system— aeroelastic—analyses. The forced oscillation cases (Cases 1 and 3b) were also performed using rigid simulations. For this particular model, where the oscillating structure is much stiffer than the mount system, this assumption is thought to be reasonable.

## IV. Workshop Participation

Sixteen analysis teams from eleven nations participated by providing computational results for the workshop. The analysis teams, organizations and configurations analyzed by each team are listed in Table 4. In this second workshop, several aerodynamic theories were used.

Many aerodynamic codes lack the fluid-structure coupling capability that is required to capture the interaction of the aerodynamics and the structural dynamics. The unsteady aerodynamic aspect of the computations is viewed as difficult, even without the added complexity of coupling to the structure. Some analysis teams chose to limit their workshop contributions to rigid forced simulations.

Table 5 lists the aerodynamic methods and tools employed and indicates whether they were used in a coupled or

**Table 3. AePW-2 Workshop Cases.**

	Case #1	Case #2	Optional Case #3au	Optional Case #3b	Optional Case #3c
Mach	0.7	0.74	0.85	0.85	0.85
AoA	3°	0°	5°	5°	5°
Dynamic Data Type	Forced Oscillation $f = 10\text{Hz}$ , $ \theta =1^\circ$	Flutter	Unforced Unsteady	Forced Oscillation $f = 10\text{Hz}$ , $ \theta =1^\circ$	Flutter
Notes:	- Attached flow - OTT exp. data - R-134a	- Flow state(?) - PAPA exp. data - R-12	- Separated flow - OTT exp. data - R-134a	- Separated flow - OTT exp. data - R-134a	- Separated flow - No exp. data - R-134a

uncoupled manner. In this paper, “coupled” refers to coupling between the structure and the fluid. Note that in Table 5, if a code is listed as coupled, it was also generally used to perform analyses for the structurally rigid cases also.

For the workshop results, the simplest aerodynamic theory employed was the doublet lattice aerodynamic methodology, described by Albano and Rodden,<sup>22</sup> Giesing, Kalman and Rodden<sup>23</sup> and Blair,<sup>24</sup> as implemented in MSC NASTRAN.<sup>25</sup> Doublet lattice is a panel method which involves solving the linearized aerodynamic potential equation derived from Euler’s equations for inviscid compressible unsteady flow. In the implementation utilized, the coupled aeroelastic equations were solved using the p-k method.<sup>26</sup>

The doublet lattice method remains the industry workhorse for aeroelastic analysis. It is also the primary method employed in the design environment when aeroelasticity is considered. Two teams provided results using this method, although others performed similar analyses to guide the solution processes for higher fidelity methods. There are many methods for improving doublet lattice predictions, by implementing correction factors based on either empirical data or on CFD. Several of these methods were implemented by team B in Table 4.

The majority of the analysis teams utilized Reynolds Averaged Navier-Stokes (RANS) flow solvers. RANS equations are time-averaged equations of motion for fluid flow. The time-averaged assumptions involve separation of chaotic velocity fluctuations from the mean flow velocity. This in turn requires the use of a turbulence model which is usually tuned for a specific flow physics situation. The unforced system analyses were in general performed by converging the RANS solutions to steady state. The forced oscillation simulations and the dynamic aeroelastic simulations (flutter simulations) were performed using unsteady RANS (URANS) codes, solved in a time-accurate manner with subiterations to converge the solution at each of the time steps.

Three analysis teams employed higher fidelity turbulence modeling. Hybrid methods employing a RANS solution and a Large Eddy Simulation (LES) solution in different regions of the flow were used primarily to analyze Case 3, where the extent of separation may be beyond the range where application of RANS is recommended.

The final aerodynamic methodology employed in workshop calculations was the time-linearized transonic small disturbance (TSD) theory.

Establishing best practices is one of the goals of the AePW. Towards this end, most analysis teams performed simulations with more than one set of input parameters. Among the parameters varied are time step size, turbulence model and flux limiter. Several analysis teams also utilized multiple software packages. For each analysis team, subcase numbers were assigned so that the results could be quickly differentiated. These subcase definitions are given in the Appendix, Table 7.

## V. Overview of the Common Databases

The computational results have been organized into databases so that they can be compared with each other and with the experimental data. There are 14 separate databases, which are detailed in the Appendix in Table 8. The databases correspond to each of the cases given in Table 3, but further differentiate the information.

The differentiations used are by type of excitation applied to the system (unforced, forced pitch oscillation or coupling due to aeroelastic interactions) and by the type of data that is compared (time-accurate or steady state). While all of the analyses could be performed in a time-accurate manner, only forced oscillation and dynamic aeroelastic simulations are compared here with methods that incorporate the time-accurate behavior. In future comparisons and publications, this will not necessarily be the case. An exception to this is the unsteady unforced analyses of Case 3, where the unforced system was simulated in a time-accurate manner. These results are not presented here.

**Table 4. Analysis teams that participated in the 2nd Aeroelastic Prediction Workshop.**

Analysis Team Code	Analysis Team Members
A	Adam Jirasek and Mats Dalenbring (FOI) Jan Navratil (Brno University of Technology, VUT, Czech Republic)
B	Guilherme Begnini, Cleber Spode Alusio V. Pantaleo, Bruno Guaraldo Neto Guilherme O. Marcorio, Marcos H.J. Pedras and Carlos Alberto Bones (Embraer S. A.)
C	Pawel Chwalowski and Jennifer Heeg (NASA Langley Research Center)
D	Daniella E. Raveh (Technion IIT) Yuval Levy and Yair Mor Yossef (Israeli CFD Center)
E	Eirikur Jonsson, Charles A. Mader and Joaquim R.R.A. Martins (University of Michigan)
F	Marcello Righi (Zurich Institute of Applied Science)
G	Balasubramanyam Sasanapuri and Krishna Zore (ANSYS India) Robin Steed (ANSYS Canada) Eric Bish (ANSYS Inc.)
H	Eric Blades and Azariah Cornish (ATA Engineering)
I	Amin Fereidooni and Anant Grewal (NRC) Marcel Grzeszczyk (NRC, University of Toronto)
J	Bimo Prananta and Bart Eussen (NLR)
K	Eduardo Molina (ITA)
L	Cetin Kiris, Michael Barad and Jeffrey Housman (NASA ARC) Christoph Brehm (University of Arizona)
M	Patrick McGah, Girish Bhandari Alan Mueller and Durrell Rittenberg (CD-adapco)
N	Sergio Ricci and Andrea Mannarino Andrea Gadda and Giulio Romanelli (Department of Aerospace Science and Technology of Politecnico di Milano)
O	Tomer Rokita (Aerodynamics department, RD&E Division, RAFAEL)
P	Yannick Hoarau and C.-K. Huang (ICUBE, Strasbourg University, France) A. Gehri and J. Vos (CFS Engineering, Lausanne, Switzerland)



**Table 5. Aerodynamic and aeroelastic methods and codes utilized in AePW-2.**

Aerodynamic Theory	Doublet lattice	Transonic small disturbance	Euler	Reynolds-averaged Navier Stokes	Reynolds-averaged Navier Stokes	Hybrid RANS/LES
Fluid-structural coupling?	x	x	x		x	x
Code Names	MSC NASTRAN	ZTRAN	OpenFoam Aero	SU2 Aero	CFD++ FUN3D EZNSS Edge EZAir STAR-CCM+ Loci/Chem Fluent CFX SUMAD ENFLOW NSMB AeroX	Edge FUN3D EZAir

The dynamic data types and processing are described here. The first type of dynamic excitation is forced oscillation in the pitch mode. The experimental comparison data was obtained during the OTT test. The data sets shown here contain information generated by oscillating the model about its pitch axis at a single set frequency for the entire time record. Each excitation can be viewed as an angle of attack excursion about the mean angle. That is, for a  $5^\circ$  angle of attack case, with an excitation of amplitude  $1^\circ$ , the wing oscillates between  $4^\circ$  and  $6^\circ$ . Frequency response functions were calculated from the forced oscillation data and reported at the frequency of the forced excitation. In this study, only data at 10 Hz forcing frequency is used, although experimental data does exist for excitation frequencies from 1 to 30 Hz.

The second type of dynamic data is due to aeroelastic coupling. An aeroelastic system is one in which the structure and the aerodynamics act as a closed system with significant feedback between those components. In time-domain simulations, an initial perturbation is applied intentionally or through numerical noise; the subsequent response is observed and analyzed. In a linear system analysis, the coupled equations are traditionally analyzed using eigenanalysis. Unstable linear systems contain a mode or modes with positive real parts of the eigenvalues. This is equivalent to the system having negative damping or energy being extracted from the airstream and work being done on the structure. Regardless of whether the system is simulated with time-domain methods or eigenanalysis methods, the AePW-2 process for comparing the results is to compute the damping of the pitch degree of freedom at the dominant system oscillation frequency. The flutter condition is determined as the dynamic pressure corresponding to a neutrally stable pitch oscillation.

The primary dynamic data selected for the AePW-2 comparison consisted of the magnitudes and phases of frequency response functions (FRFs). The FRFs of principal interest were the pressure coefficients ( $C_p$ ) due to angular displacement. The FRF for each pressure coefficient due to pitch displacement was calculated at the frequency of the dominant response of the the pitch displacement.

Fourier analysis was performed on each dynamic data set to produce FRFs for each pressure relative to the displacement of the system. The FRFs were formed from power spectral and cross spectral densities (PSDs and CSDs), which were computed using Welch's periodogram method. The Fourier coefficients used in computing the PSDs and CSDs were generated using discrete Fourier transform (DFT) analysis of the time histories, employing overlap-averaged ensembles of the data sets. The Fourier parameters, including the length of the ensembles, the overlap percentage, the window shape and the frequency at which the data was extracted were chosen independently by each analysis team.

## VI. Collected Results

The collected results from all of the analysis teams are presented in this section, compared with experimental data where available. The data is presented by case number, as described above. For the unforced— steady— cases, the mean values of pressure coefficients are plotted as functions of non-dimensional chord location for each surface and span station. For the forced oscillation and dynamic aeroelastic cases, the frequency response functions are plotted at a single frequency as functions of non-dimensional chord location. For flutter cases, the flutter dynamic pressure and frequency are shown, identified by analysis team letter. The final section shows the integrated (lift and pitching moment) coefficients for unforced cases.

### A. Analysis Case #1: Mach 0.7, 3° angle of attack

#### 1. Comparison plots

Unforced and forced-oscillation analyses were conducted at Mach 0.7, 3° angle of attack for analysis Case 1 of the AePW-2 test cases. Experimental comparison of pressure results, obtained from the OTT test, are available for only the inboard span station for these cases.

The mean pressure coefficients are shown for the upper and lower surfaces at 60% and 95% span stations, Figure 2. The plots show different colors for each analysis team, with a different symbol for each subcase submitted. The individual analysis teams results are not separately identified in the current paper. The black symbols on the plots show the experimental data, where the circles indicate the mean values, while the triangles indicate the upper and lower 99% capture bounds (i.e., the largest and smallest 1/2% outliers are excluded from the bounds). An enlarged view of the comparison plots is shown in Figure 3 for the forward portion of the chord on the upper surface.

The frequency response functions of pressure coefficients at 60% span due to pitch angle at 10 Hz forced pitch oscillation are shown for the upper and lower surface data sets in Figure 4. Figures 4(a) and (b) show the mean values of the pressure distributions obtained from the forced oscillation simulations. Note that some analysis teams submitted FRF results without also submitting mean values extracted from those data sets. Thus, subplots (a) and (b) show fewer results than the other subplots in this figure. The FRF magnitude plots are shown in Figures 4(c) and (d) and the phase plots are shown in Figures 4(e) and (f). Figures 4(c) and (d) show the magnitude of the FRF of pressure due to angular displacement for the upper and lower surfaces, and Figures 4(e) and (f) show the corresponding phase of the FRF. Some of the data sets show a phase that is 180° out of phase with the experimental data and the majority of the computational results. It is thought that a negative sign was applied to the data for some reason during the post-processing phase, however, this has not been verified to date.

#### 2. Results discussion: mean values

The unforced system computations (Figure 2) show good agreement with the experimental data, with the possible exception of the peak value near the leading edge on the upper surface. The mean values extracted from forced oscillation data show similar good agreement with experiment, except again in the same region near the leading edge. It is curious to note that the shape formed by the bounds of the experimental forced oscillation data resemble the shape of the computational data produced by the unforced simulations, and vice versa. In making comparisons between the experiment and the computations, it is important to recall from the first workshop lessons learned: the mean value of the pressure coefficient does a poor job of representing the data in the shock region. This lesson likely also applies to the leading edge region where large changes in pressure coefficient are produced by very small perturbations.

The two experimental data sets (unforced and mean value extracted from forced oscillation) are plotted together in Figure 5. In this figure, the bounds of the experimental data are represented in a more obvious manner than in the earlier figures. The mean value of the unforced experiment data is shown with red symbols and the range of the data is shown by the red error bars. The blue symbols and lines show the corresponding results for the forced pitch oscillation experiment data set.

There are several observations to make regarding the unforced vs. forced pressure distribution. At first inspection, the shapes of the pressure distributions produced by these two types of simulations appear different. The unforced system does not appear to have much of a supersonic plateau region. That is, the shock is barely formed for this test condition. The forced system data represents the shock over a wider chord-wise range, but that plateau is mainly formed due to shock movement, rather than actual width of the shock at any point in time. This can be observed using a smear plot of the time history data, but is also indicated by the erratic mean value at different chord locations and the fact that the unforced system response peak is near the center of the forced oscillation cases shock range of motion.



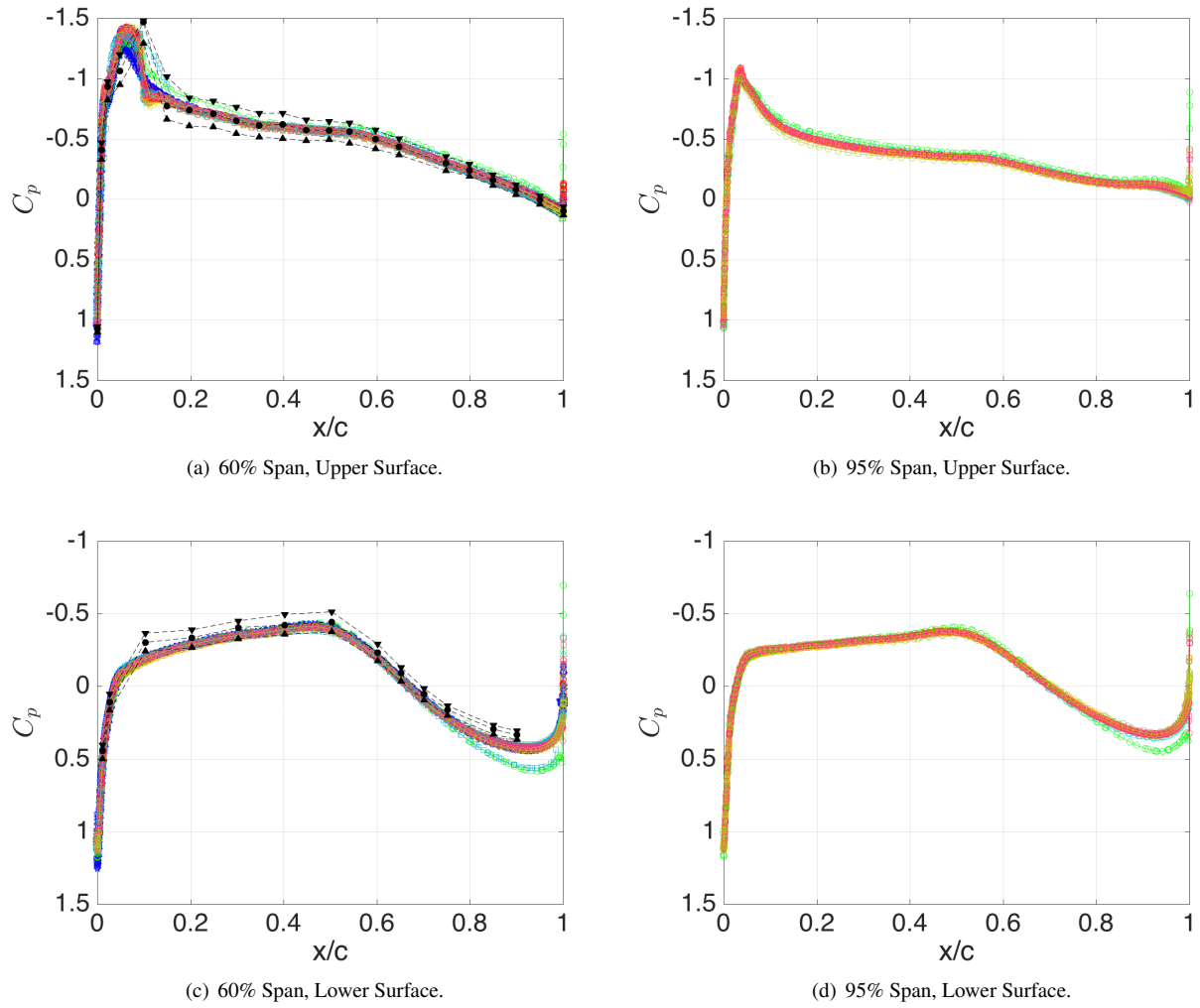


**Figure 2. Case 1 (Mach 0.7,  $Re_c = 4.49 \times 10^6$ ,  $\alpha = 3^\circ$ ): Mean  $C_p$  for Unforced System data. Colors show computational results, by team. Black symbols show experimental data.**

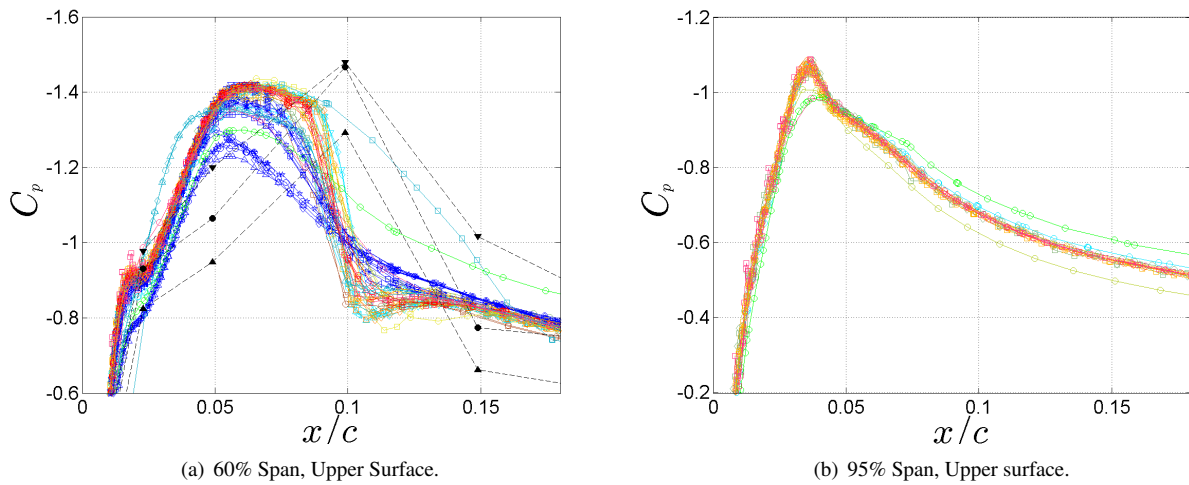
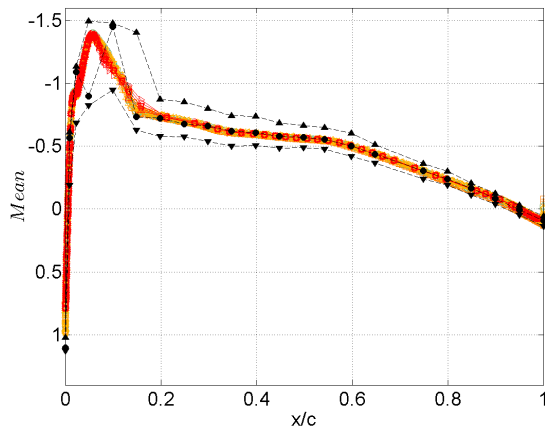
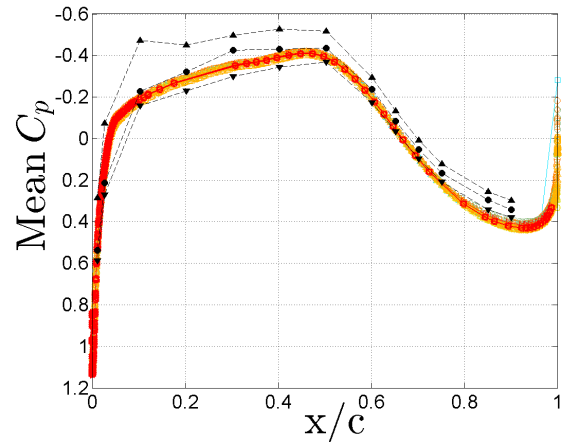


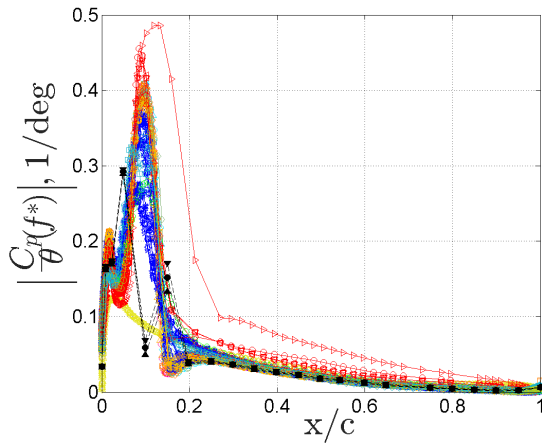
**Figure 3. Mean  $C_p$ : Enlarged views of the upper surface shock region for unforced simulation: Case 1 (Mach 0.7,  $Re_c = 4.49 \times 10^6$ ,  $\alpha = 3^\circ$ ). Colors show computational results, by team. Black symbols show experimental data.**



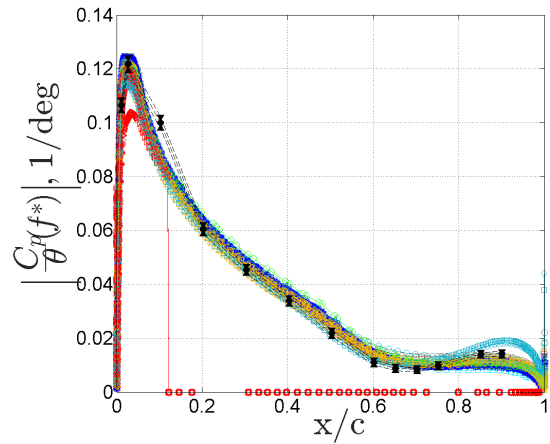
(a) Mean  $C_p$ , Upper Surface.



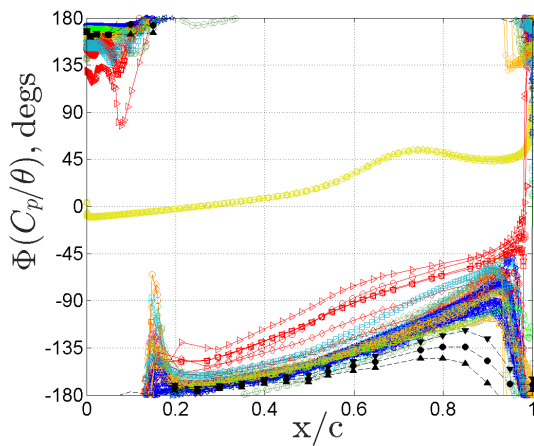
(b) Mean  $C_p$ , Lower Surface



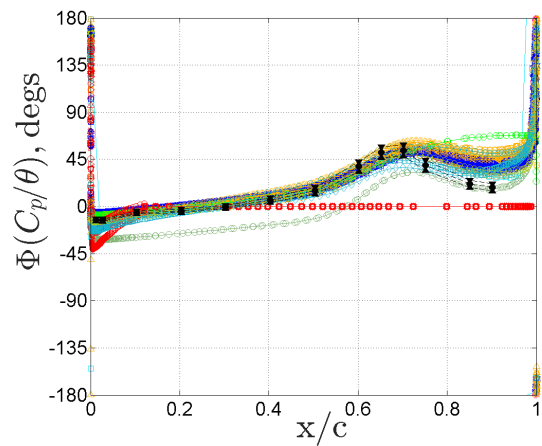
(c) Magnitude of  $C_p/\theta$ , Upper Surface.



(d) Magnitude of  $C_p/\theta$ , Lower Surface



(e) Phase  $C_p/\theta$ , Upper Surface.



(f) Phase  $C_p/\theta$ , Lower Surface.

**Figure 4. Comparison Data for Case 1 (Mach 0.7,  $q = 204$  psf, Forced oscillation at 10Hz,  $Re_c = 4.49 \times 10^6$ ,  $\alpha = 5^\circ$ ): Frequency Response Function of Pressure Due to Pitch Angle, 60% Wing Span. Colors show computational results, by team. Black symbols show experimental data.**

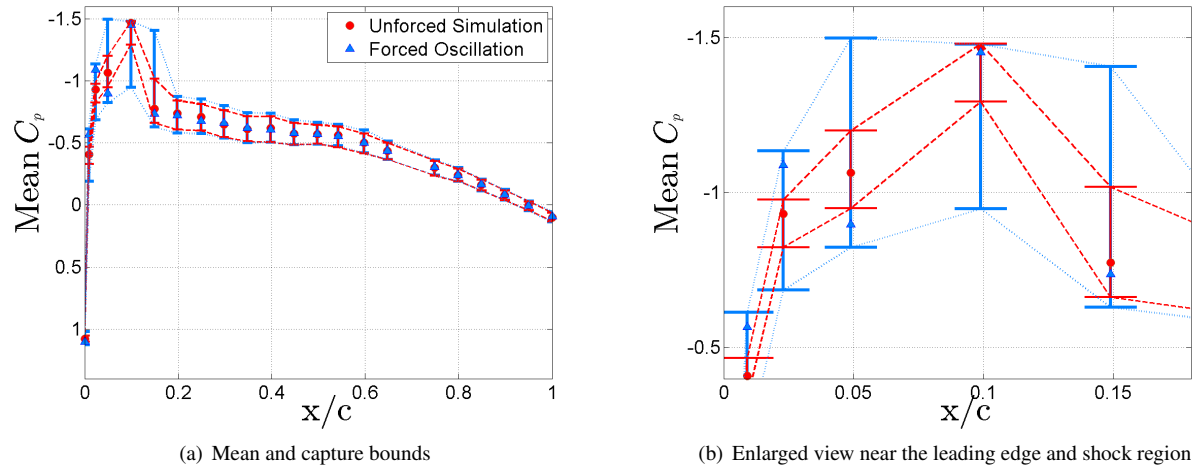


**Figure 5. Experimental data. Mean Value and Capture Bounds of  $C_p$  for Unforced and Forced Oscillation Simulations: Case 1 (Mach 0.7,  $q = 204$  psf,  $f = 10$  Hz,  $Re_c = 4.49 \times 10^6$ ,  $\alpha = 5^\circ$ ): Upper surface, 60% Wing Span.**

Note that the forced systems bounds exceed the unforced systems bounds only in the forward region of the airfoil. Over the aft portion of the wing (from approximately  $x/c = 0.25$  to the trailing edge), the mean values and the bounds are nearly identical for the two cases.

Another point to note is that the mean value does not properly capture the most likely values of the pressure coefficients over this forward portion of the chord. From a mathematical standpoint, this is because the distribution of the values are not Gaussian distributed. From a physics standpoint, this is due to the shock moving across the grid points or pressure transducers which toggles the pressure coefficient between the value associated with the supersonic plateau and the value associated with the foot of the shock. Note how the mean value is very near the upper bound for some points and very near the lower bound for other points.

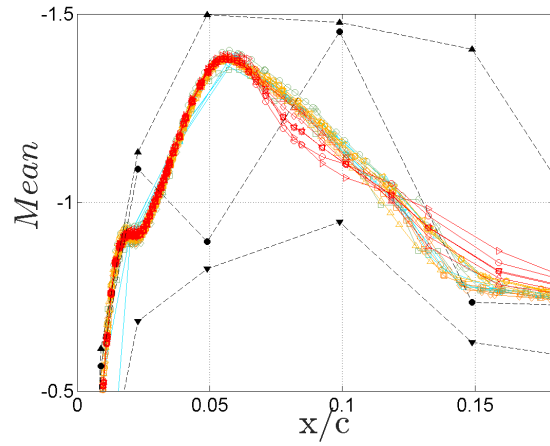
### 3. Results discussion: FRFs

The connection between the mean pressure distribution and the frequency response function can be seen by examining these plots in more detail. The data for the upper surface at 60% span station is discussed. As seen in Figures 4(c) and 6(b), the frequency response function magnitude has two dominant peaks, near  $x/c = 0.09$  and  $0.02$ .

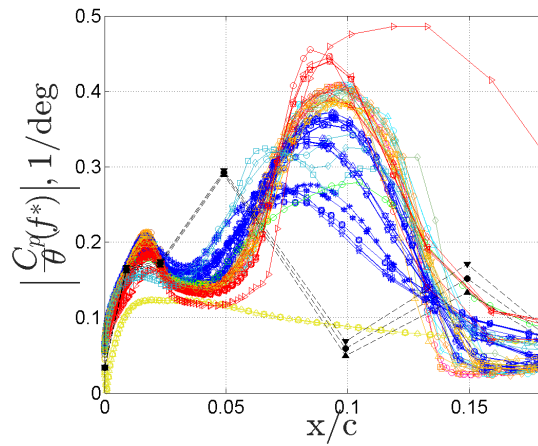
The dominant peak near  $x/c = 0.09$  corresponds to the movement of the upper surface shock. The forced oscillation amplitude is  $1^\circ$ , so during the forced oscillation, the angle of attack moves through approximately  $2^\circ$ . For this analysis case the flow is in general attached, so as the angle of attack increases, the shock shifts aft and vice versa. The magnitude peak is at the same location as the maximum change in pressure coefficient. This is not always true since the FRF is calculated at a specific frequency and the range of the static pressure coefficient values would be just as large for a single near-static sweep through the values.

As the wing pitches leading edge upward, the shock moves aft and the pressure coefficient values decrease for points ahead of the shock. That is, on the supersonic plateau, the pressure coefficient is dropping with increasing angle of attack. Note that on the customary inverted scale showing the pressure coefficient, this is seen as the plateau rising. This means that the pressure coefficient and the pitch angle are out of phase, i.e., phased  $180^\circ$  relative to each other. This is seen in the phase plots of the FRFs in Figure 4(c).

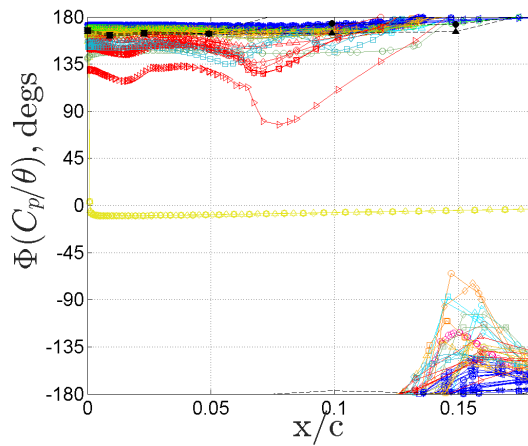
The secondary peak, near  $x/c = 0.02$  chord, indicates the influence of the flow acceleration around the airfoil leading edge. The pressure peak moves and resizes with the changing angle of attack. For this analysis case, the mean angle of attack is  $3^\circ$ , thus the range of oscillation for this case is from  $2$  to  $4^\circ$ . On the upper surface near the  $x/c = 0.02$  chord, the local geometric shape of the airfoil is more bulbous and introduces a local acceleration of the flow and corresponding decreased pressure in this region, shown as a small hump in all plots of the upper surface pressure distribution for this case.



(a) Mean  $C_p$



(b)  $|C_p/\theta|$



(c) Phase, degs.

**Figure 6. Forced Oscillation Data for Case 1 (Mach 0.7,  $q = 204$  psf,  $f = 10$ Hz,  $Re_c = 4.49 \times 10^6$ ,  $\alpha = 5^\circ$ ): Upper surface, 60% Wing Span, magnifying near the leading edge. Colors show computational results, by team. Black symbols show experimental data.**

## B. Analysis Case #2: Mach 0.74 and 0° angle of attack

The second AePW-2 test case focuses on flutter prediction at Mach 0.74 and 0° angle of attack. Data generated at different steps in the analysis process are also compared. These steps include rigid unforced system analyses, static aeroelastic analyses and time-accurate aeroelastic analysis at the experimental flutter condition. These are viewed as likely steps that most analysis teams would have taken in getting to the flutter onset prediction, but they were not required steps. Some teams chose to go immediately to a time-accurate, dynamic, coupled simulation, without running an overdamped analysis to produce an estimate of the static aeroelastic system.

Experimental comparison results, obtained from the PAPA test, are available at both the 60% and 95% span station. The experimental flutter onset dynamic pressure was measured in the wind tunnel as 168.8 psf, where the model responded at a flutter frequency of 4.3 Hz.

The mean pressure coefficients are shown for the upper and lower surfaces at 60% and 95% span stations, Figure 7. Rather than showing the data for each analysis team as a separate color, the plotted data uses a different color to represent three static system analyses: rigid unforced, static aeroelastic at the experimental flutter condition, and static aeroelastic at the computational flutter condition. Note that each analysis predicted different flutter onset conditions, so the results presented for that case represent different dynamic pressures. The black symbols on the plots show the experimental data for the unforced rigidized mount system data point. The circles indicate the mean values, while the triangles indicate the upper and lower 99% capture bounds (i.e., the largest and smallest 1/2% outliers are excluded from the bounds).

Figures 8 and 9 show the comparison data for the dynamic flutter simulations and experiment at the two span stations at 168.8 psf. This is the dynamic pressure of flutter onset found in during the experiment. The mean value from the dynamic data are shown in subplots (a) and (b) of each figure. The FRF magnitudes for the upper and lower surfaces are shown in subplots (c) and (d), respectively. The phase of the FRFs are shown in subplots (e) and (f). The experimental data is shown again by the black symbols, with the nominal values shown by the circles. The upper and lower bounds for the experiment show coherence-based uncertainty estimates.

Figures 10 and 11 show the comparison data for the dynamic flutter simulations and experiment at the two span stations at the predicted flutter onset dynamic pressures. The mean value from the dynamic data are shown in subplots (a) and (b) of each figure. The FRF magnitudes for the upper and lower surfaces are shown in subplots (c) and (d), respectively. The phase of the FRFs are shown in subplots (e) and (f). The computational results are again shown by the colored data sets, where each color corresponds to a different analysis team. Each of the computational results shown here corresponds to a different dynamic pressure, i.e., the dynamic pressure where each predicted flutter onset.

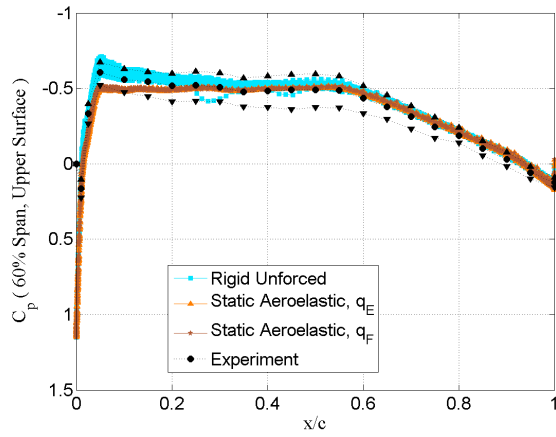
## C. Analysis Case #3: Mach 0.85 at 5° angle of attack

The BSCW case from AePW-1 was Mach 0.85 at 5° angle of attack at a dynamic pressure of 204 psf. The AePW-1 results showed significant scatter in the data reported by the different analysis teams. To continue working the problem in the hope of resolving these discrepancies, this case became an optional case for the AePW-2 workshop.

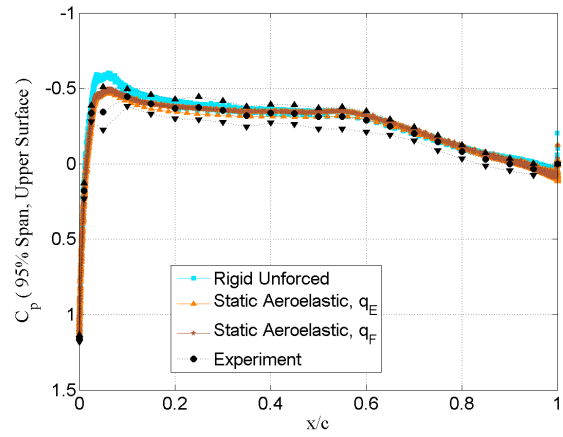
Based on the AePW-1 results and recommendations from the community, three analysis subcases were formulated at this test condition. The first subcase (Case 3au) assessed the rigid-steady versus rigid-unsteady flow calculations in the presence of the shock-induced separated flow, which dominates the upper surface and the aft portion of the lower surface. Results for this subcase are not presented in this paper. The second subcase (Case 3b), computed the flow around the wing undergoing forced oscillation at 10 Hz. For both of these subcases, experimental data is available at the inboard span station. The most challenging workshop case was the so, it is considered to be a flutter onset prediction at this condition (Case 3c). Unfortunately, experimental data does not exist for this case. It is considered here as a “blind” prediction case.

The mean pressure coefficients are shown for the upper and lower surfaces at 60% and 95% span stations, Figure 12. As in Case 2, the plotted data uses a different color to represent three static system analyses: rigid unforced, static aeroelastic at the experimental flutter condition, and static aeroelastic at the computational flutter condition. Again, note that each analysis predicted different flutter onset conditions, so the results presented for that case represent different dynamic pressures. The black symbols on the plots show the experimental data for the unforced rigidized mount system data point. The circles indicate the mean values, while the triangles indicate the upper and lower 99% capture bounds (i.e., the largest and smallest 1/2% outliers are excluded from the bounds).

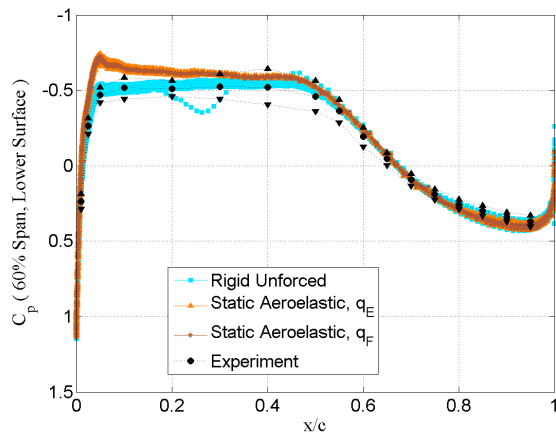
Figure 13 shows the comparison data for the 10 Hz forced pitch oscillation case at 204 psf, at the 60% span station. The mean pressure coefficient values from the dynamic data are shown in subplots (a) and (b) for the upper and lower surfaces, respectively; the magnitudes of the FRF of pressure due to angular displacement are shown in subplots (c) and (d); and the phase of the corresponding FRFs are shown in subplots (e) and (f). The experimental data



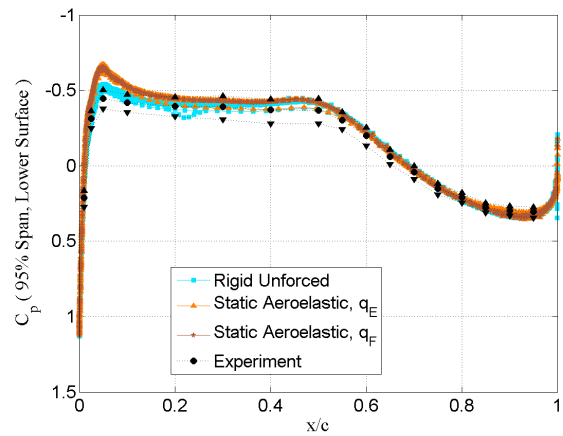
(a) 60% Span, Upper Surface.



(b) 95% Span, Upper Surface.



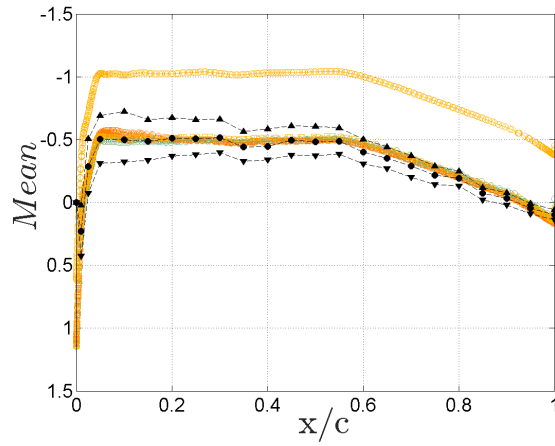
(c) 60% Span, Lower Surface.



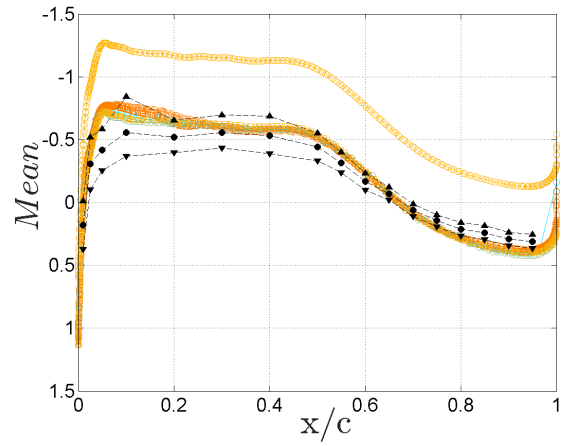
(d) 95% Span, Lower Surface.

**Figure 7. Case 2 (Mach 0.74  $Re_c = 4.49 \times 10^6$ ,  $\alpha = 0^\circ$ ): Mean  $C_p$  for Unforced System data sets.**

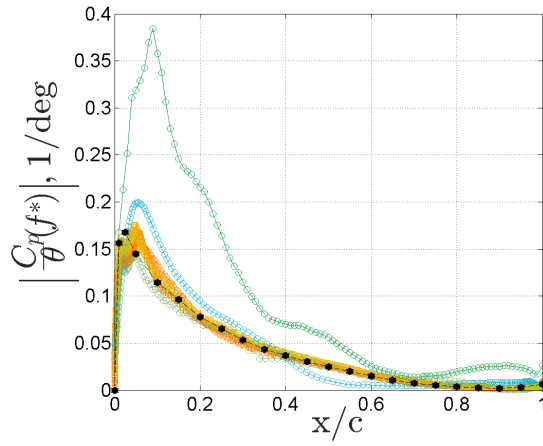




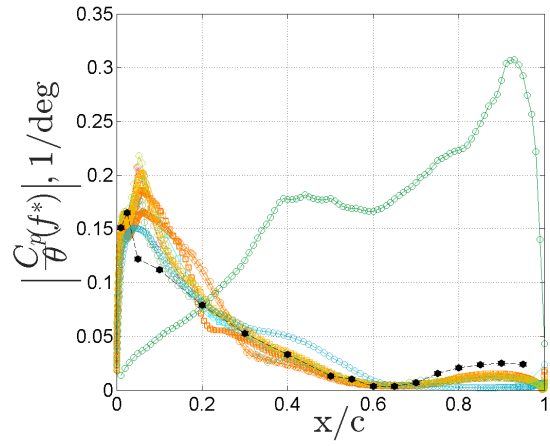
(a) Mean  $C_p$ , Upper Surface.



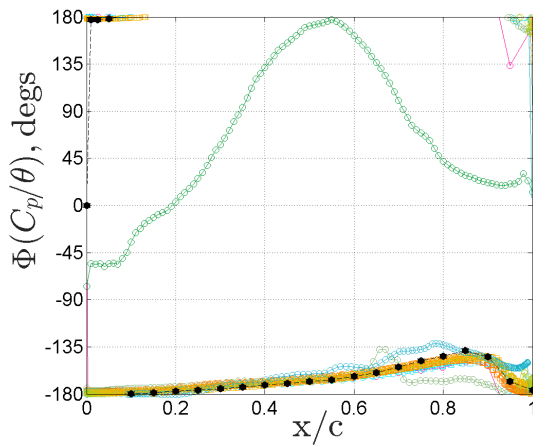
(b) Mean  $C_p$ , Lower Surface



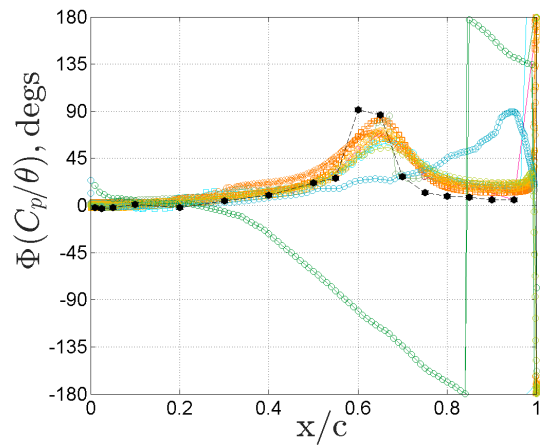
(c) Magnitude of  $C_p/\theta$ , Upper Surface.



(d) Magnitude of  $C_p/\theta$ , Lower Surface

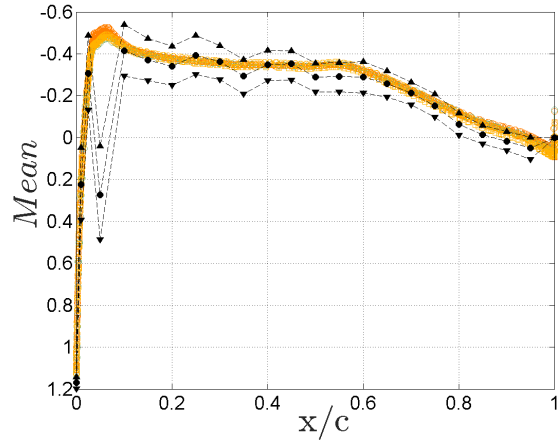


(e) Phase  $C_p/\theta$ , Upper Surface.

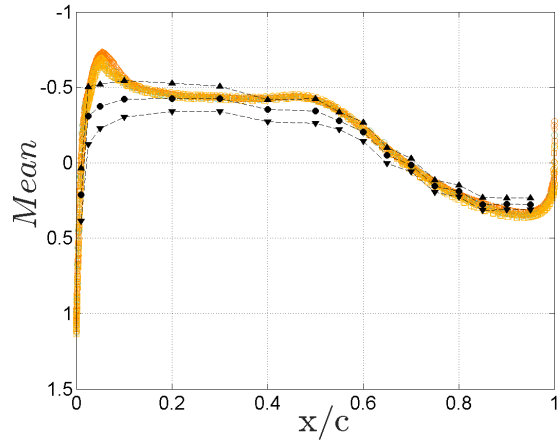


(f) Phase  $C_p/\theta$ , Lower Surface.

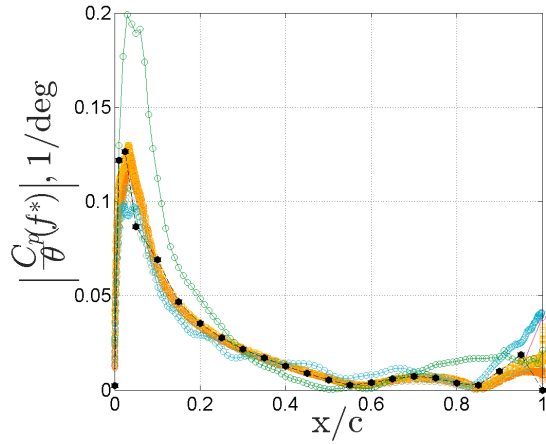
**Figure 8. Comparison Data for Case 2, Coupled Aeroelastic Response at the Experimental Flutter Dynamic Pressure, FRFs at the System Primary Response Frequency (Mach 0.74,  $q = 204$  psf,  $Re_c = 4.49 \times 10^6$ ,  $\alpha = 5^\circ$ ): Frequency Response Function of Pressure Due to Pitch Angle, 60% Wing Span.**



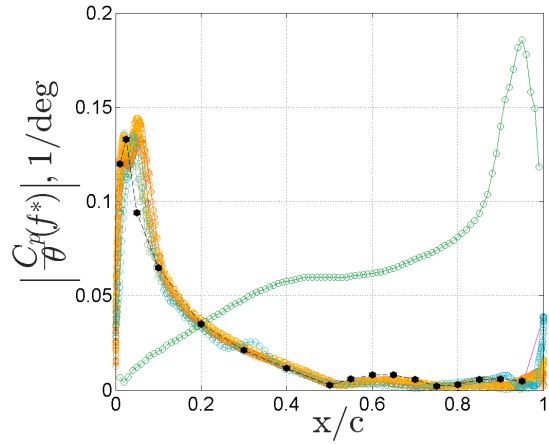
(a) Mean  $C_p$ , Upper Surface.



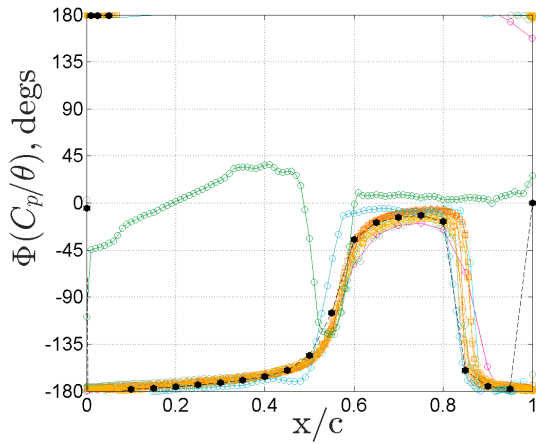
(b) Mean  $C_p$ , Lower Surface



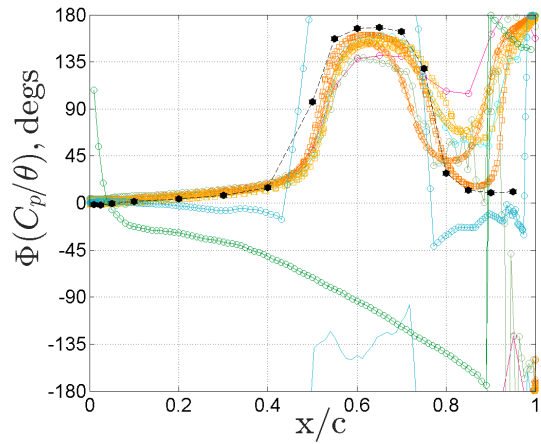
(c) Magnitude of  $C_p/\theta$ , Upper Surface.



(d) Magnitude of  $C_p/\theta$ , Lower Surface

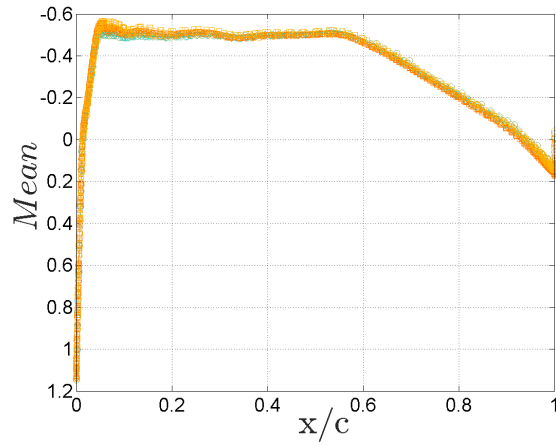


(e) Phase  $C_p/\theta$ , Upper Surface.

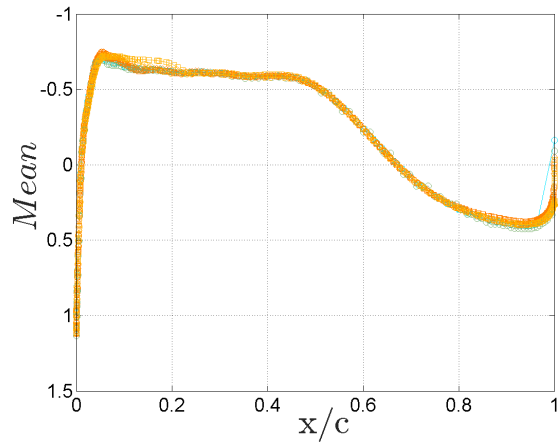


(f) Phase  $C_p/\theta$ , Lower Surface.

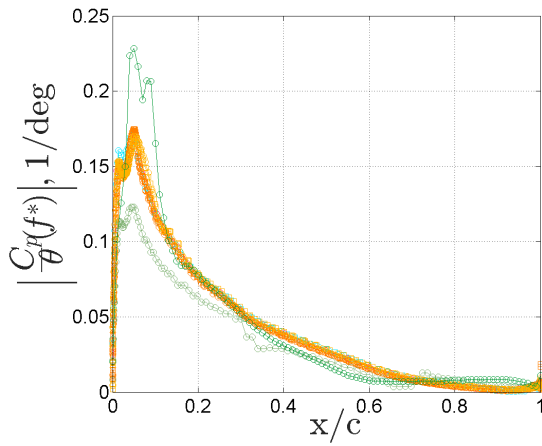
**Figure 9. Comparison Data for Case 2, Coupled Aeroelastic Response at the Experimental Flutter Dynamic Pressure, FRFs at the System Primary Response Frequency (Mach 0.74,  $q = 204$  psf,  $Re_c = 4.49 \times 10^6$ ,  $\alpha = 5^\circ$ ): Frequency Response Function of Pressure Due to Pitch Angle, 95% Wing Span. Each color corresponds to a different analysis team, not individually identified.**



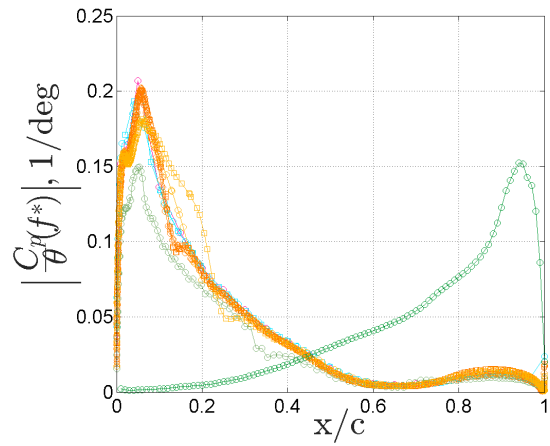
(a) Mean  $C_p$ , Upper Surface.



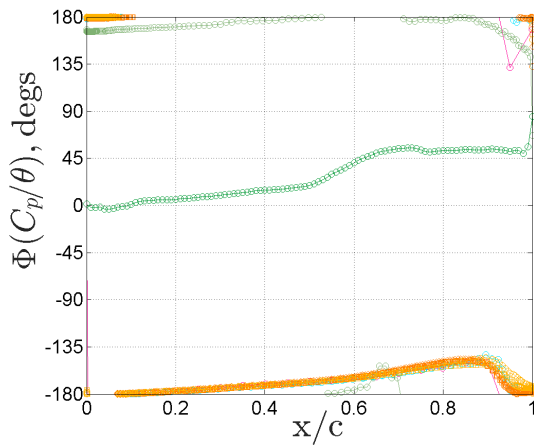
(b) Mean  $C_p$ , Lower Surface



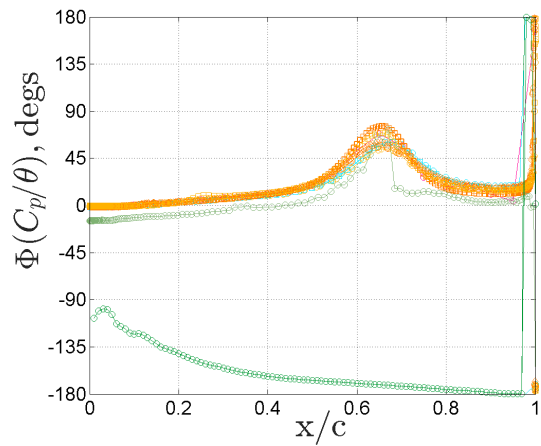
(c) Magnitude of  $C_p/\theta$ , Upper Surface.



(d) Magnitude of  $C_p/\theta$ , Lower Surface

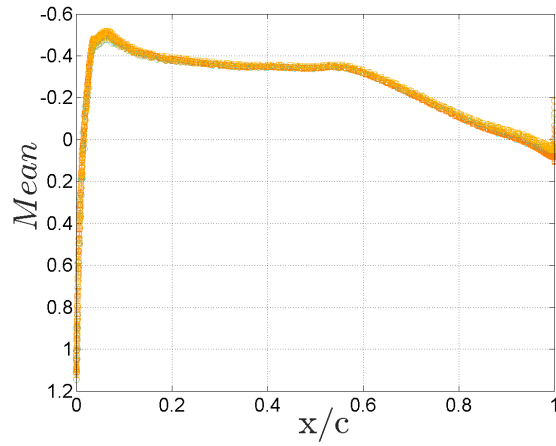


(e) Phase  $C_p/\theta$ , Upper Surface.

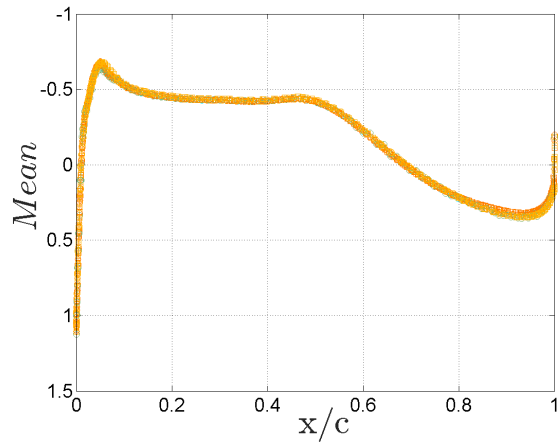


(f) Phase  $C_p/\theta$ , Lower Surface.

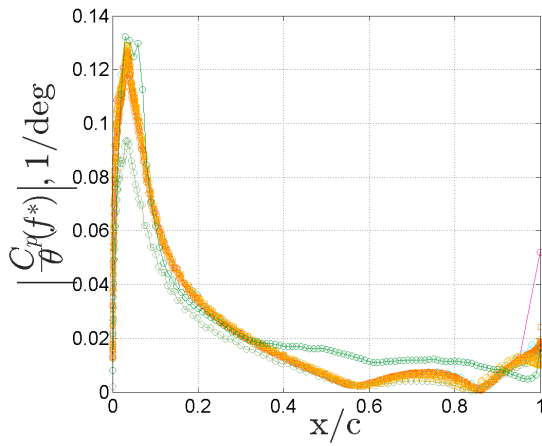
**Figure 10. Comparison Data for Case 2, Coupled Aeroelastic Response at the Predicted Flutter Dynamic Pressure, FRFs at the System Primary Response Frequency (Mach 0.74,  $Re_c = 4.49 \times 10^6$ ,  $\alpha = 5^\circ$ ): Frequency Response Function of Pressure Due to Pitch Angle, 60% Wing Span.**



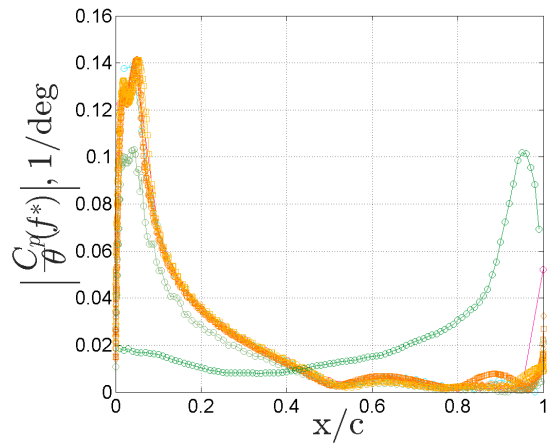
(a) Mean  $C_p$ , Upper Surface.



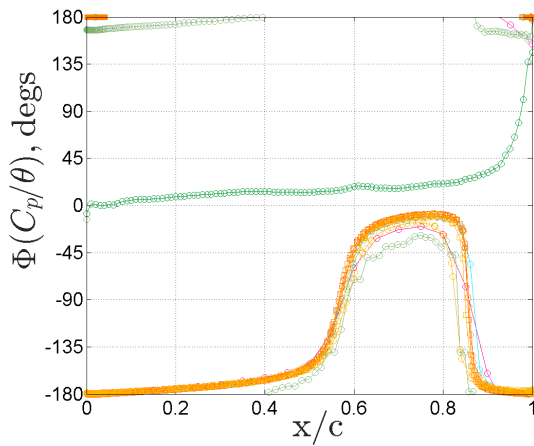
(b) Mean  $C_p$ , Lower Surface



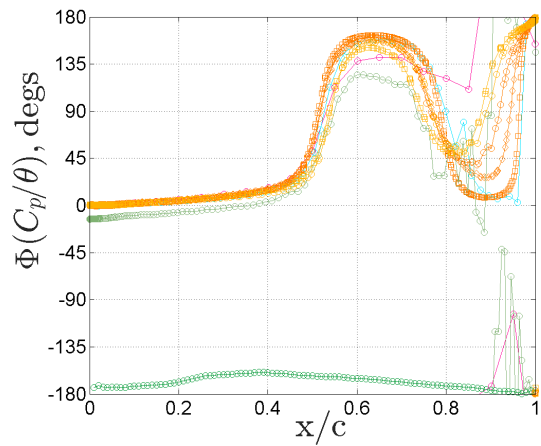
(c) Magnitude of  $C_p/\theta$ , Upper Surface.



(d) Magnitude of  $C_p/\theta$ , Lower Surface



(e) Phase  $C_p/\theta$ , Upper Surface.



(f) Phase  $C_p/\theta$ , Lower Surface.

**Figure 11. Comparison Data for Case 2, Coupled Aeroelastic Response at the Predicted Flutter Dynamic Pressure, FRFs at the System Primary Response Frequency (Mach 0.74,  $Re_c = 4.49 \times 10^6$ ,  $\alpha = 5^\circ$ ): Frequency Response Function of Pressure Due to Pitch Angle, 95% Wing Span.**

is shown again by the black symbols, with the nominal values shown by the circles. The upper and lower bounds for the experiment show coherence-based uncertainty estimates.

Figure 14 shows the comparison data for the dynamic coupled aeroelastic simulations and experiment at 204 psf, at the 60% span station. Figure 15 shows the comparison data for the dynamic coupled aeroelastic simulations at the flutter onset condition, at the 60% span station. The ordering of the information remains the same as in the previous plots: (a) and (b) show the mean pressure coefficient values; (c) and (d) show the FRF magnitudes; and (e) and (f) show the FRF phases. There is no experimental data available for comparison to these computational results.

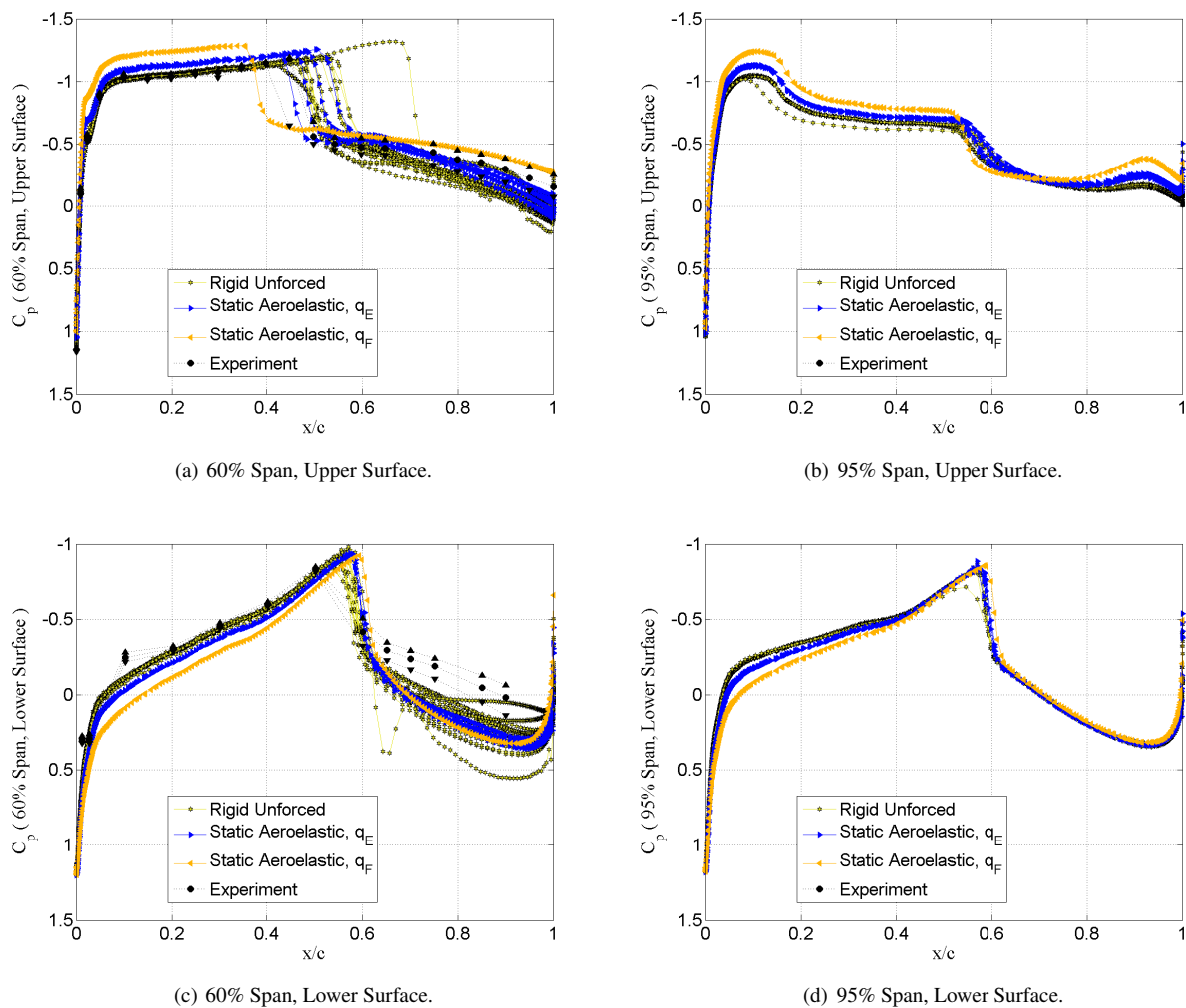


**Figure 12. Case 3 (Mach 0.85  $Re_c = 4.49 \times 10^6$ ,  $\alpha = 5^\circ$ ): Mean  $C_p$  for Unforced System data sets.**

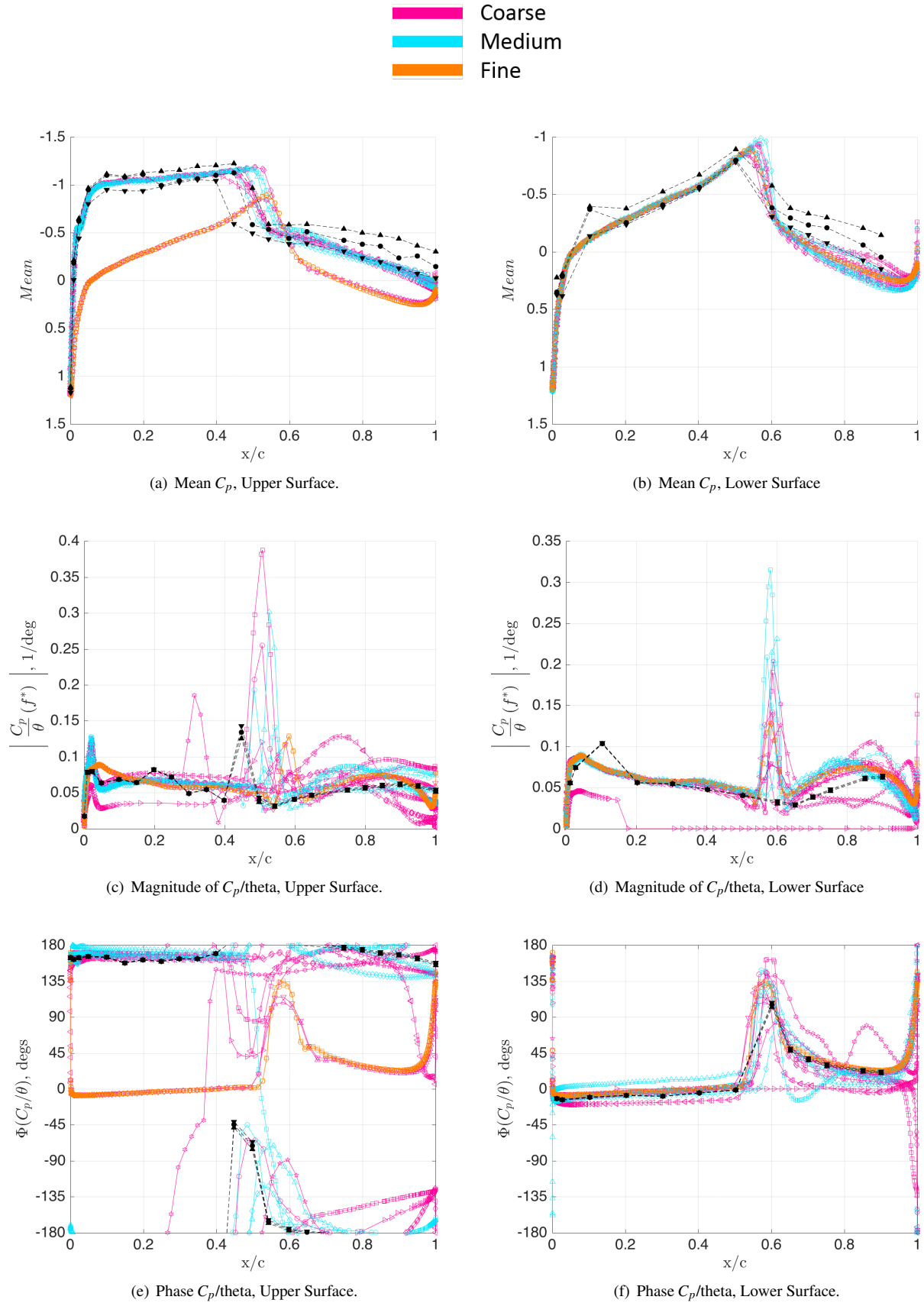


**Figure 13. Comparison Data for Case 3, FRFs at the Forcing Frequency, 10 Hz. Forced Oscillation at the common analysis condition, (Mach 0.85,  $q = 204$  psf,  $Re_c = 4.49 \times 10^6$ ,  $\alpha = 5^\circ$ ): Frequency Response Function of Pressure Due to Pitch Angle, 60% Wing Span. Colors indicate grid resolution.**



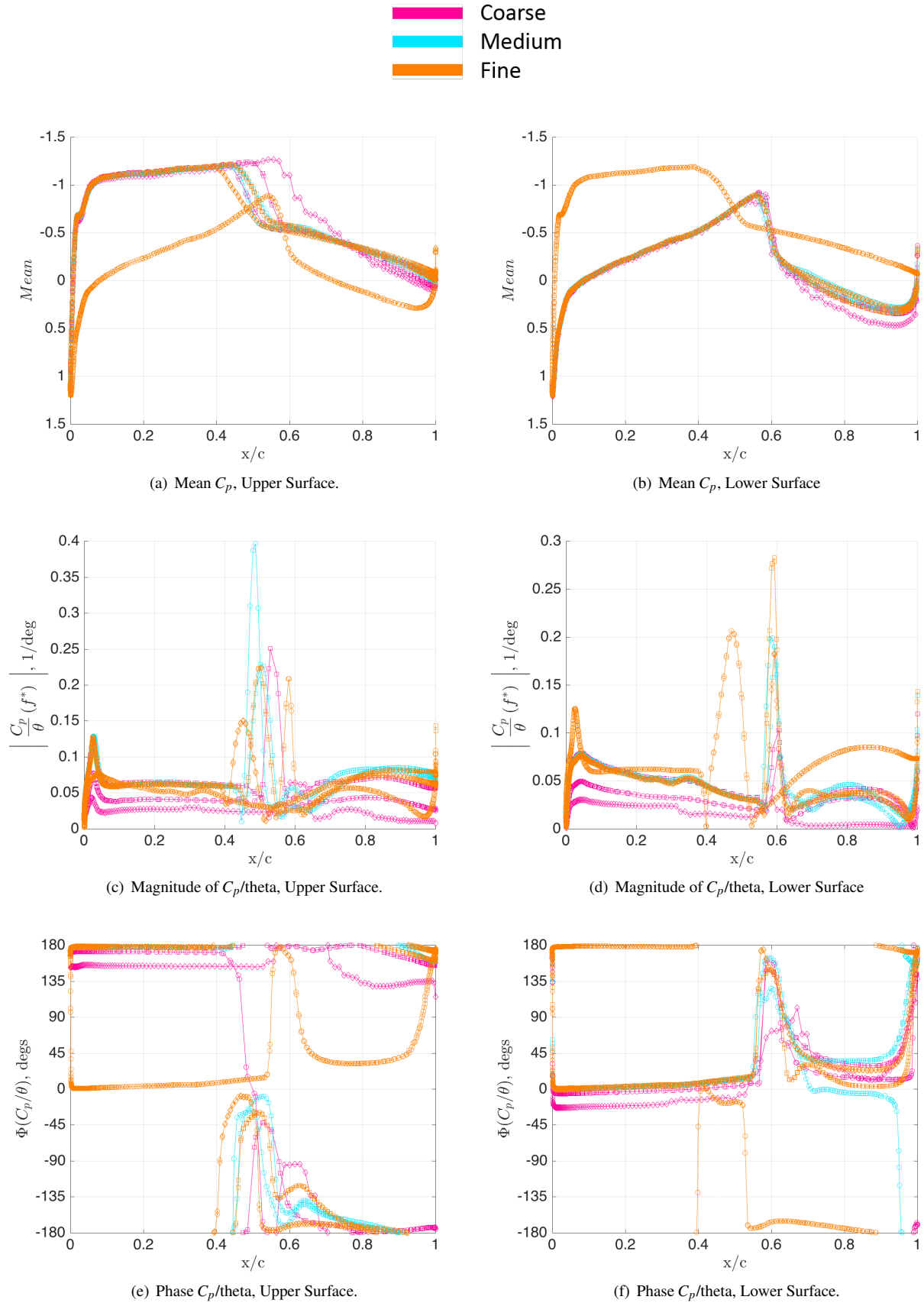


**Figure 14. Comparison Data for Case 3, FRFs at the Primary System Response Frequency. Coupled Aeroelastic Response at the the common analysis condition, (Mach 0.85,  $q = 204$  psf,  $Re_c = 4.49 \times 10^6$ ,  $\alpha = 5^\circ$ ): Frequency Response Function of Pressure Due to Pitch Angle, 60% Wing Span. Colors indicate grid resolution.**

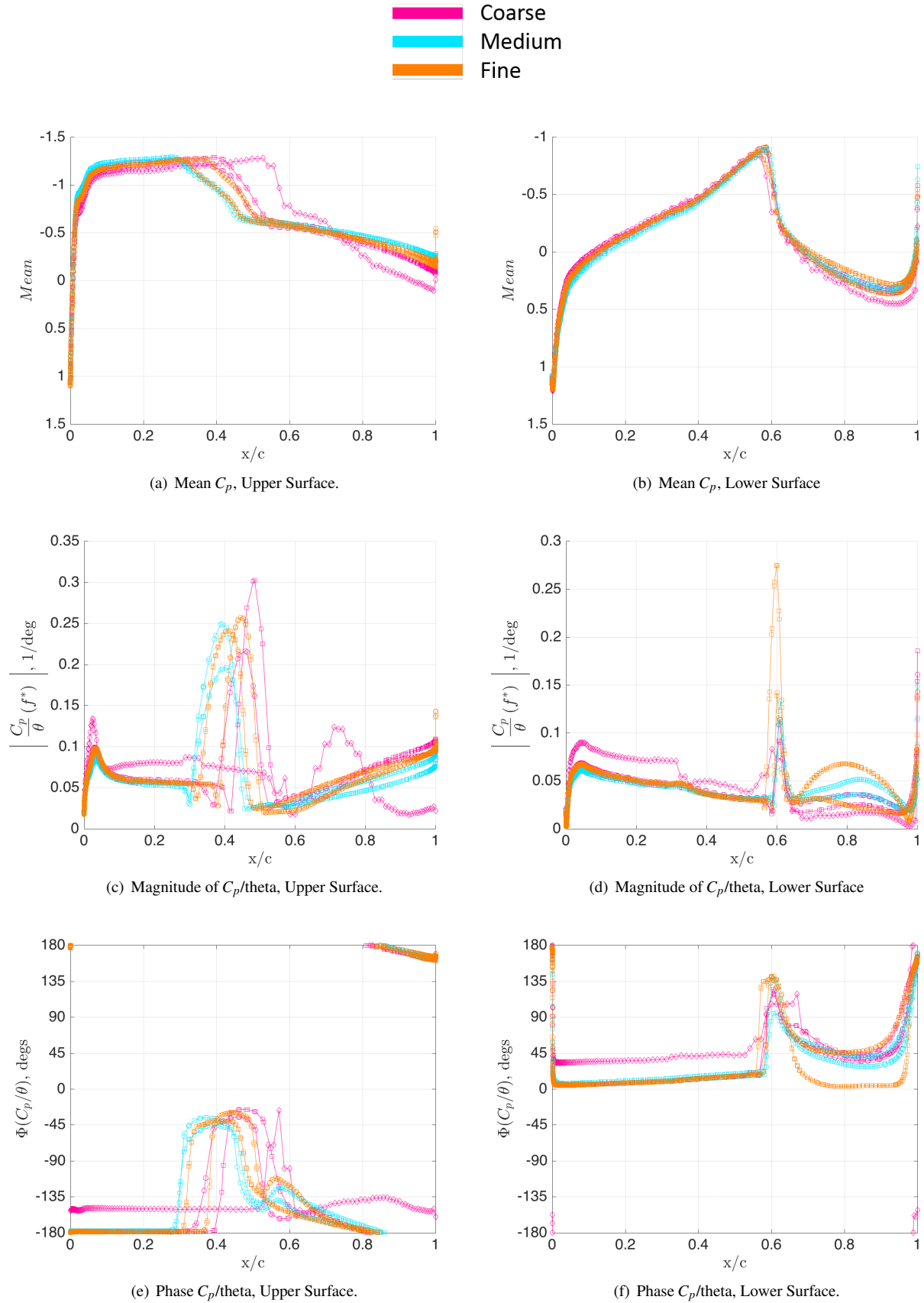


**Figure 15. Comparison Data for Case 3, FRFs at the Primary System Response Frequency. Coupled Aeroelastic Response at the computationally predicted flutter dynamic pressure, (Mach 0.85,  $\alpha = 5^\circ$ ): Frequency Response Function of Pressure Due to Pitch Angle, 60% Wing Span. Colors indicate grid resolution.**

## VII. Static Aeroelastic Results

The predicted static aeroelastic pitch angles are shown in Figure 16. The lift and pitching moment coefficients are presented in Figure 17 for all three analysis conditions, although Case 1 results contains no static aeroelastic effects. Each row of plots shows the lift and pitching moment coefficients for a different analysis condition. The lift coefficients are shown in the left hand column (subplots (a), (c) and (e)); the pitching moment coefficients are shown in the right hand column (subplots (b), (d) and (e)). Additional data sets were collected for the drag coefficient and sectional coefficients at the 60% and 95% span stations, but are not presented here. The data points are shown as functions of grid factor, defined here as the number of nodes or cells to the  $-2/3$  power. In the plots, the analysis types—rigid unforced, static aeroelastic at the experimental flutter onset condition, and static aeroelastic at the computational flutter onset condition—are differentiated by the colors and symbols.

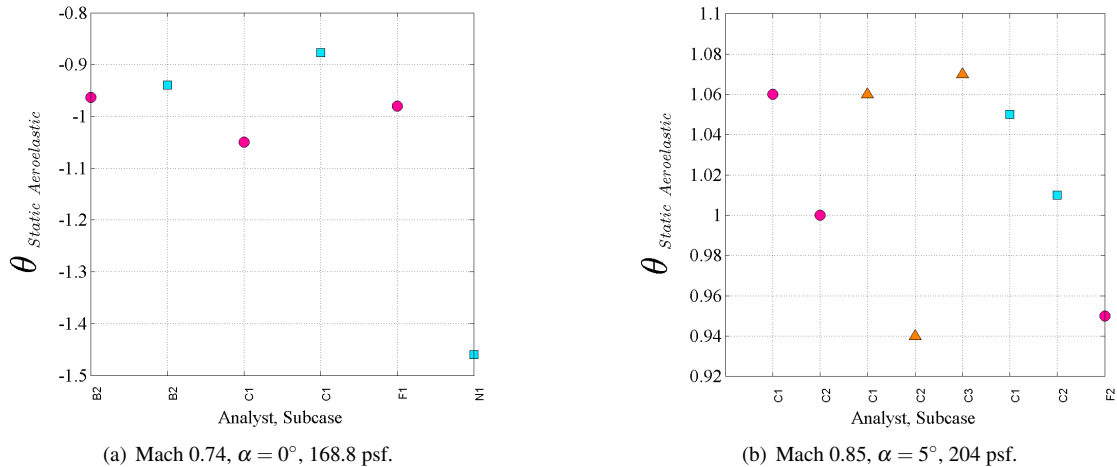


Figure 16. Static aeroelastic twist angle at the experimental dynamic pressure, identified by analysis team and subcase.

## VIII. Flutter Results

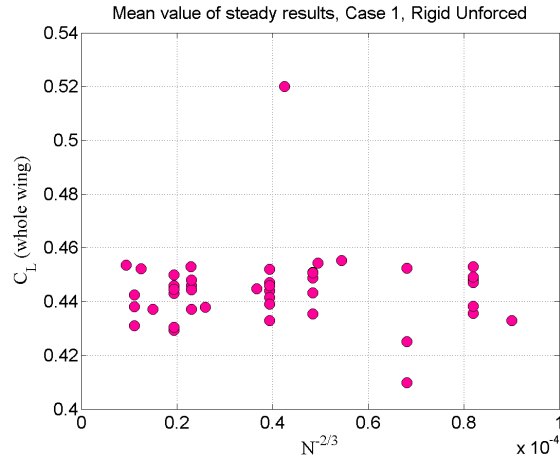
### A. Comparison plots

Results from the flutter predictions are presented in Figure 18 for Case 2, and in Figure 19 for Case 3. In both Figures, subplot (a) shows the predicted flutter onset dynamic pressure and subplot (b) shows the predicted frequency of the flutter mechanism. In each plot, the horizontal axis shows the analysis team letter (refer to Table 4) and the corresponding subcase number (refer to Table 7). The symbols indicate the grid resolution (coarse, medium, fine and extra fine). These grid resolution definitions were made based on the provided grids and the gridding guidelines. For the computations where the provided grids were utilized, these definitions correspond to the number of nodes as listed in Table 6. Other grids were left to the analysis team to assess regarding the labels of coarse, medium, fine and extra fine. The linear analyses are indicated by a separate symbol, as identified in the legend.

Also shown in the Figure for Case 2 are the experimental flutter onset dynamic pressure and the experimental flutter frequency.

Table 6. Grid resolution definitions of the provided unstructured grids for AePW-2.

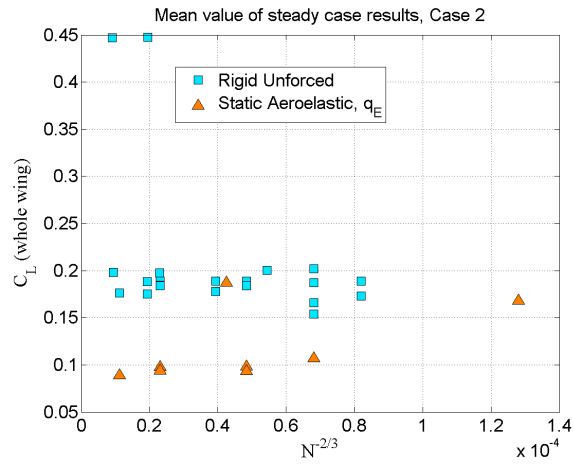
Resolution	Number of Nodes
Coarse	2968550
Medium	9005346
Fine	26786862
Xtra Fine	78324474



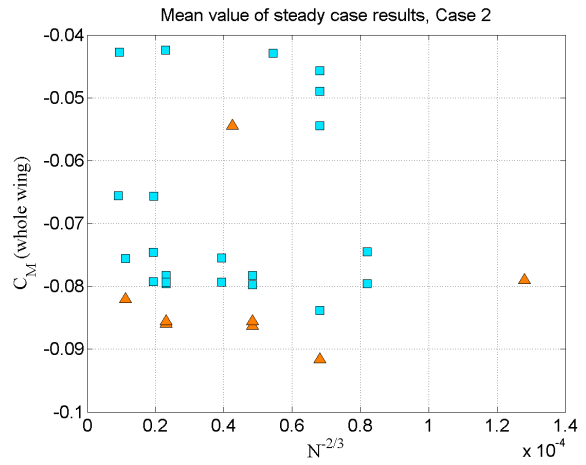
(a)  $C_L$ , Case 1: Mach 0.7,  $\alpha = 3^\circ$ .



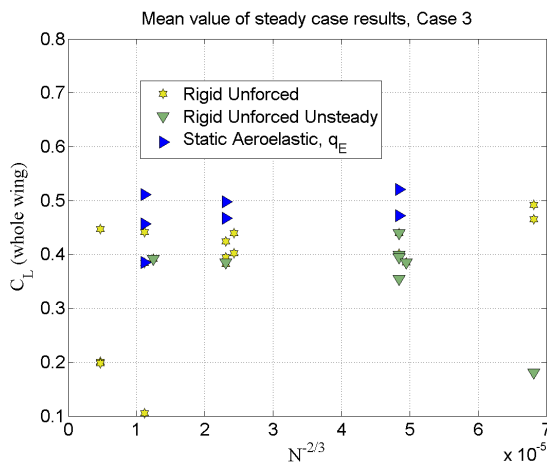
(b)  $C_M$ , Case 1: Mach 0.7,  $\alpha = 3^\circ$ .



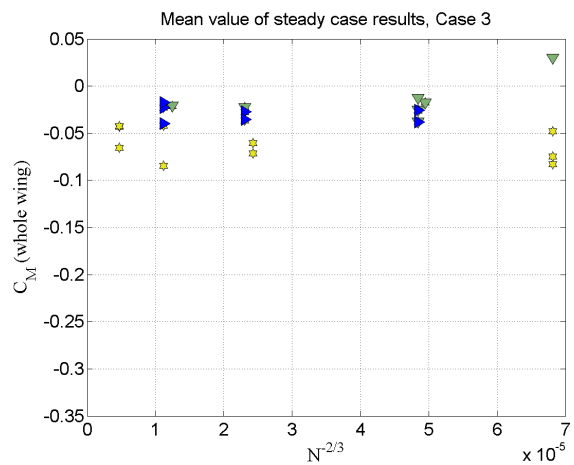
(c)  $C_L$ , Case 2: Mach 0.74,  $\alpha = 0^\circ$ .



(d)  $C_M$ , Case 2: Mach 0.74,  $\alpha = 0^\circ$ .

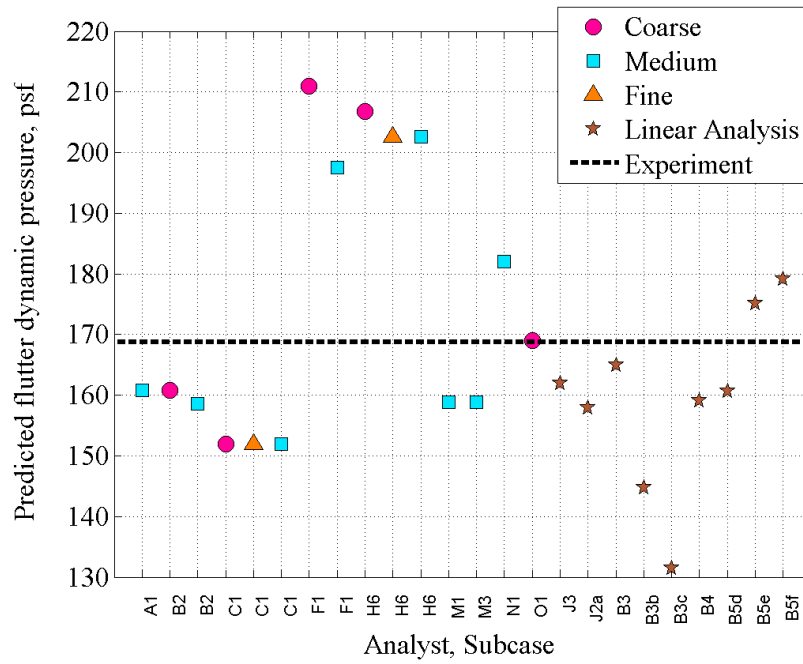


(e)  $C_L$ , Case 3: Mach 0.85,  $\alpha = 5^\circ$ .

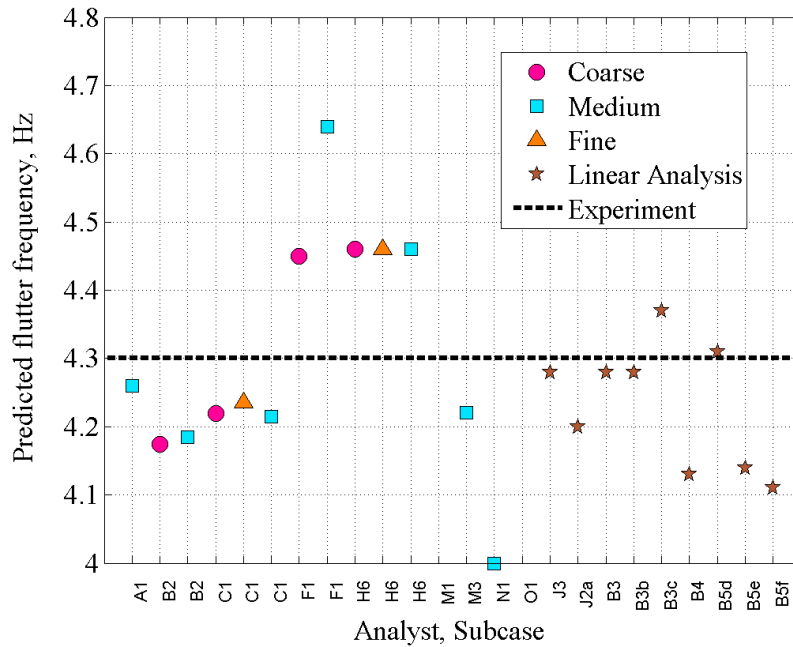


(f)  $C_M$ , Case 3: Mach 0.85,  $\alpha = 5^\circ$ .

**Figure 17. Mean values of integrated coefficients.**

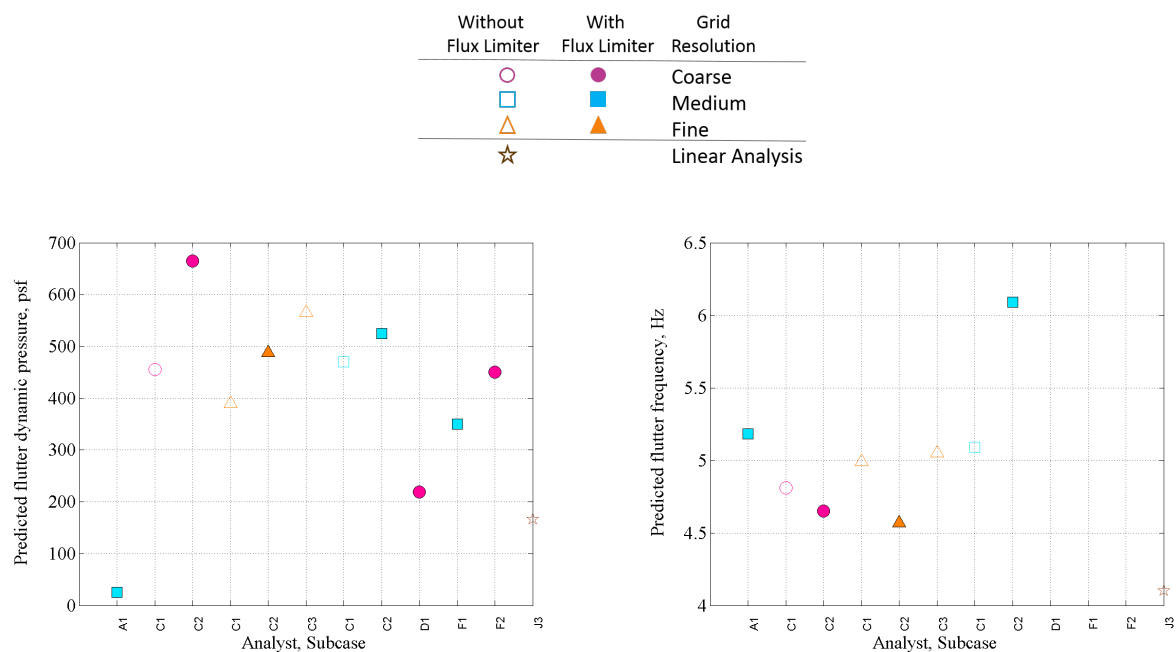


(a) Flutter dynamic pressure identified by analysis team and subcase.



(b) Flutter dynamic pressure identified by analysis team and subcase.

**Figure 18. Flutter Results for Case 2:Mach 0.74,  $\alpha = 0^\circ$ .**



(a) Flutter dynamic pressure identified by analysis team and subcase. (b) Flutter dynamic pressure identified by analysis team and subcase.

**Figure 19. Flutter Results for Case 3: Mach 0.85,  $\alpha = 5^\circ$ , showing the influence of using a flux limiter.**

## B. Results discussion

The predictions of the flutter onset condition for Case 2 are fairly well grouped, lying in a range from 131 to 207 psf, which is a range of 44% of the experimental dynamic pressure. While the mean value taken over all results (165.4 psf) is quite close to the experimental flutter condition (168.8 psf), the standard deviation of the results is 18.6 psf. Using the experimental value as the reference, the mean value has an error of 2%, and it is considered to be conservative. Using the range of values obtained, the worst case predictions in each direction (non-conservative meaning underpredicting; and non-conservative meaning overpredicting) had errors of 22%.

There are several points to consider. The first point is that the experimental flutter dynamic pressure was known prior to performing simulations. This is useful to use as a guide in setting up the range of parameters for the analyses, but perhaps has too strong of an influence on when an analysis team decides that their solution has converged. The second point is that the flow conditions are considered to be relatively benign. This case was well-predicted by the linear methods. The linear analyses, taken as a separate group, produce a mean value (159.5 psf) that has a greater error (5.5%) but is more conservative. The grouped linear analysis results also have less variation, indicated by a lower standard deviation (14.4 psf).

The predictions for flutter onset for Case 3 are wildly varying. At Mach 0.85,  $5^\circ$  angle of attack, analysis of the experimental data and results from the first workshop indicate that there is shock-boundary-layer interaction on the upper surface, generating separated flow over much of the airfoil. The lower surface also sees separated flow from the cusp region aft. This is a challenging flow field to predict, even without the fluid-structure coupling. The predicted results range from flutter onset near 25 psf up to flutter onset at 665 psf. This case lacks experimental data to guide the analyst. Additionally, linear prediction methods don't incorporate the influence of angle of attack. Here, the uncorrected doublet lattice results gave 166 psf as the flutter onset prediction.

For Case 2, there was an observed correspondence between static aeroelastic twist angle and dynamic pressure increases. That is, for aeroelastic analysis data sets where results were submitted at multiple dynamic pressures, a higher dynamic pressure always generated an increased magnitude of the static aeroelastic twist angle.

In the current paper, the results have not been presented sorted by analysis input parameters because few trends have been observed to date. One exception is the dependence of the flutter dynamic pressure on the use of a flux limiter. The Case 3 flutter dynamic pressure is presented in Figure 19 showing the differences observed in companion analyses with and without flux limiter. In the figure, open symbols show the cases without a flux limiter, while filled symbols show the cases with a flux limiter. A flux limiter introduces additional numerical damping into the simulation, generating a data set with higher combined damping, and thus higher dynamic pressure predictions for flutter onset.



The comparison data sets represent one aspect of the workshop accomplishments. Arguably as important is the content of the discussions held at the workshop. A few points that arose during those discussions are summarized here. A significant change from the first workshop was the focus on temporal parameter effects and convergence relative to these choices. While these issues haven't been thoroughly explored at this point in time, almost all computational teams examined their solutions to see the effects of time step size on the prediction of aeroelastic stability. Using a common method to define temporal convergence was discussed. The combined spatial- and temporal-convergence issue was touched on and many people agreed that it is an issue. A simplified test case to examine the confounded convergence issue thoroughly was proposed.

Members of most computational teams were in agreement that the procedures used in arriving at a prediction for the flutter onset condition are improvisational and inefficient. Suggested methods to explore for improving the process included the use of reduced order models, sensitivity-based approaches, alternate excitation simulations, and indicative parameter selection. Arriving at a solution was made easier if an estimate of the condition was provided by experimental data. Linear methods, such as doublet lattice and strip theory, were also used to produce quick estimates to guide the solution process. Speaking only for the authors of the current paper, although we were thorough in our parameter space exploration, the confidence with which we declared the solution to be good enough was definitely influenced by the presence of experimental results for Case 2.

The question was also discussed: How do we assess the accuracy of a stability prediction? The discussion centered on trying to understand and discern numerical vs. physical damping in a simulation. The influence of using a flux limiter was briefly explored by the NASA team, showing that including the additional damping associated with employing a flux limiter has the predictable effect of making the aeroelastic simulation more stable (i.e., less flutter-prone). The broader issue of stability assessment requires additional attention.

There are several issues centered around post processing. The post processing required to extract time-correlated, time-accurate spatially-distributed information and organize it into a data set is excessive. Also, the comfort level in executing the required processes was low. Both the execution and the low comfort level are in contrast to the handling of "steady" data.<sup>a</sup> For "steady" data examination, there are generally well-established code-internal processes that calculate spatially integrated coefficients, such as lift, drag and pitching moment.

## IX. Concluding Remarks

Much of the comparison data from the 2nd AIAA Aeroelastic Prediction Workshop has been presented in this paper. There are still results to examine such as frequency response functions using integrated coefficients as the response variables, the sectional lift and pitching moment coefficient data and detailed time histories. The data submitted for the workshop comparisons is a small fraction of the information generated in reaching these data sets. Much work remains to be done to understand why the simulations give such varied predictions of flutter onset. Much work remains to be done to understand which underlying physics are being correctly or incorrectly predicted, and which are critical in terms of predicting aeroelastic system behavior.

## Acknowledgments

The authors thank the BSCW computational teams who contributed computational results to AePW-2, and the members of the workshop organizing committee. The authors also thank the NASA Transformational Tools and Technologies Project and the NASA Engineering and Safety Center for their sponsorship of this work.

## References

- <sup>1</sup>Schuster, D., Chwalowski, P., Heeg, J., and Wieseman, C., "A summary of data and findings from the first Aeroelastic Prediction Workshop," Tech. rep., Hawaii, 2012, 7th International Conference on Computational Fluid Dynamics, ICCFD7-2012.
- <sup>2</sup>Heeg, J., Chwalowski, P., Florance, J., Wieseman, C., Schuster, D., and Perry, B., I., "Overview of the Aeroelastic Prediction Workshop," AIAA-2013-0783, 51st AIAA Aerospace Sciences Meeting, Grapevine, TX, Jan 2013.
- <sup>3</sup>Heeg, J., Chwalowski, P., Schuster, D., Dalenbring, M., Jirasek, A., Taylor, P., Mavriplis, D., Boucke, A., Ballmann, J., and Smith, M., "Overview and lessons learned from the Aeroelastic Prediction Workshop," IFASD-2013-1a, Bristol, UK, 2013.

---

<sup>a</sup>The word "steady" has a dictionary general usage definition of "showing little variation or fluctuation"<sup>27</sup> or "free from fluctuation."<sup>28</sup> Assigning the term "steady" to a case implies that nothing is changing in time. Is the snapshot taken at the end of a simulation a good representation of the data? Only if the case is truly not varying with time. Is the mean value taken over a range of time points a good representation of the data? Only if the data is Gaussian distributed.

- <sup>4</sup>Chwalowski, P., Heeg, J., Dalenbring, M., Jirasek, A., Ritter, M., and T., H., "Collaborative HiReNASD analyses to eliminate variations in computational results," IFASD-2013-1d, Bristol, UK, 2013.
- <sup>5</sup>Prananta, B., B., E., van Muijden, J., Heeg, J., Atik, H., and Wieseman, C., "Analysis of First AIAA Aeroelastic Prediction Workshop results of unforced and oscillating HiReNASD wing," IFASD-2013-2b, Bristol, UK, 2013.
- <sup>6</sup>Sens, A.-S., "Comparison of aeroelastic solutions on the HiReNASD model," IFASD-2013-11a, Bristol, UK, 2013.
- <sup>7</sup>Boucke, A., "Uncertainties in Measurements and Data Evaluation Concerning Transonic High Reynolds Number Wind Tunnel Tests," IFASD-2013-38c, Bristol, UK, 2013.
- <sup>8</sup>Schuster, D., Chwalowski, P., Heeg, J., and Wieseman, C., "Analysis of test case computations and experiments from the first aeroelastic prediction workshop," AIAA-2013-0788, 51st AIAA Aerospace Sciences Meeting, Grapevine, TX, Jan 2013.
- <sup>9</sup>Mavriplis, D., Yang, Z., Long, M., and Sitaraman, J., "Results using NSU3D for the first aeroelastic prediction workshop," AIAA-2013-0786, 51st AIAA Aerospace Sciences Meeting, Grapevine, TX, Jan 2013.
- <sup>10</sup>Chwalowski, P., Heeg, J., Wieseman, C., and J.P., F., "FUN3D analyses in support of the first aeroelastic prediction workshop," AIAA paper 2013-0784, 51st AIAA Aerospace Sciences Meeting, Grapevine, TX, Jan 2013.
- <sup>11</sup>Raveh, D., Yossef, Y., and Levy, Y., "Flow simulations for the first aeroelastic prediction workshop using the EZNSS Code," AIAA-2013-0787, 51st AIAA Aerospace Sciences Meeting, Grapevine, TX, Jan 2013.
- <sup>12</sup>Dalenbring, M., Jirasek, A., Chwalowski, P., and Heeg, J., "Initial Investigation of the BSCW Configuration using Hybrid RANS-LES modeling," Tech. rep., 2013, AIAA-2013-1801, 54th AIAA/ASME/ASCE/AHS/ASC Structures, Structural Dynamics, and Materials Conference, Boston, Massachusetts, Jan. 8-11, 2013.
- <sup>13</sup>Nikbay, M. and Acar, P., "Steady and Unsteady Aeroelastic Computations of HiReNASD Wing for Low and High Reynolds Numbers," AIAA-2013-1800, 2013, 54th AIAA/ASME/ASCE/AHS/ASC Structures, Structural Dynamics, and Materials Conference, Boston, Massachusetts, Jan. 8-11, 2013, doi:10.2514/6.2013-1800.
- <sup>14</sup>Wieseman, C., Chwalowski, P., and Heeg, J., "Structural Dynamics Modeling of HiReNASD in Support of the Aeroelastic Prediction Workshop," AIAA-2013-1801, 2013, 54th AIAA/ASME/ASCE/AHS/ASC Structures, Structural Dynamics, and Materials Conference, Boston, Massachusetts, Jan. 8-11, 2013.
- <sup>15</sup>Heeg, J., Chwalowski, P., Wieseman, C., Florance, J., and Schuster, D., "Lessons learned in the selection and development of test cases for the first aeroelastic prediction workshop: Rectangular Supercritical Wing," AIAA-2013-0784, 51st AIAA Aerospace Sciences Meeting, Grapevine, TX, Jan 2013.
- <sup>16</sup>Heeg, J., Chwalowski, P., Schuster, D. M., Raveh, D., Jirasek, A., and Dalenbring, M., "Plans and Example Results for the 2nd AIAA Aeroelastic Prediction Workshop," AIAA Paper 2015-0437, Jan 2015.
- <sup>17</sup><http://aaac.larc.nasa.gov/tsab/cfdlarc/aiaa-dpw/>, August 2010.
- <sup>18</sup><http://hiliftpw.larc.nasa.gov/>, August 2010.
- <sup>19</sup>Rumsey, C. and Lee-Rausch, E., "The NASA Juncure Flow Experiment: Goals, Progress, and Preliminary Testing," AIAA Paper 2016-1557, San Diego, 2016, Presented at AIAA SciTech Meeting, 4-8 January 2016, San Diego, California, USA; 54th AIAA Aerospace Sciences.
- <sup>20</sup>Schuster, D. M., "Aerodynamic Measurements on a Large Splitter Plate for the NASA Langley Transonic Dynamics Tunnel," NASA TM 2001-210828, March 2001.
- <sup>21</sup>Heeg, J. and Piatak, D., "Experimental data from the Benchmark SuperCritical Wing wind tunnel test on an oscillating turntable," AIAA-2013-1801, 2013, 54th AIAA/ASME/ASCE/AHS/ASC Structures, Structural Dynamics, and Materials Conference, Boston, Massachusetts, Jan. 8-11, 2013.
- <sup>22</sup>Albano, E. and Rodden, W., "A Doublet-Lattice Method for Calculating Lift Distributions on Oscillating Surfaces in Subsonic Flows," *AIAA Journal*, Vol. 7, No. 2, 1969, pp 279-285.
- <sup>23</sup>Giesing, J., Kalman, T., and Rodden, W., "Subsonic unsteady aerodynamics for general configurations, Part I, Vol I, Direct application of the nonplanar doublet lattice method," Air Force Technical Report AFFDL-TR-71-5, 1971.
- <sup>24</sup>Blair, M., "A compilation of the mathematics leading to the doublet lattice method," Air Force Wright Laboratory Technical Report WL-TR-92-3028, 1992.
- <sup>25</sup>MSC Software, Santa Ana, CA, *MSC Nastran*, 2008, "[http://www.mscsoftware.com/products/msc\\_nastran.cfm](http://www.mscsoftware.com/products/msc_nastran.cfm)".
- <sup>26</sup>Hassig, H. J., "An approximate true damping solution fo the flutter equation by determinant iteration," *Journal of Aircraft*, Vol. 8, No. 11, Nov 1971.
- <sup>27</sup><http://www.merriam webster.com>, *Merriam Webster Online*, Merriam-Webster, Incorporated, 2015.
- <sup>28</sup><http://www.collinsdictionary.com/dictionary/english>, *Collins Dictionary Online*, HarperCollins Publishers Limited, 2016.

## **X. Appendix: Comparison Data Details**

Table 7 lists the software and several parameters for results reported in the comparison data sets. The subcase numbers given in the table correspond to the plot labels seen throughout this report. Note that in defining the subcases, if only a single value of a parameter is used by an analysis team, it is listed only once. When analysis teams provided results at multiple time step sizes, a separate subcase was defined for tracking the non-time-accurate (steady) results. For these cases, the time step is listed as ‘none.’ Where values were not provided by analysis teams, the value is listed as ‘unknown.’

Table 8 describes the 14 database files that have been generated and contain the comparison data sets for AePW-2.

**Table 7. Parameter variations for submitted comparison results; Assignment of subcase numbers.**

Analyst Code	Subcase Number	Software Name	Turbulence Model	Flux Limiter	Time Step (sec)
A	1	EDGE	SA	unknown	1.00E-04
	2		DDES	unknown	1.00E-04
B	1	CFD++	k-omega SST	TVD	7.80E-04
	2	Aero	SA	van Albada	0.0001
	3a	NASTRAN (uncorrected)		none	none
	3b	NASTRAN (derivative correction)			
	3c	NASTRAN (pre-diagonal correction)			
	4	ZTRAN		none	unknown
	5a	Euler (linearized Qhh)		none	unknown
	5b	Euler (linearized time domain)			
	5c	Euler (nonlinear time domain)			
C	1	FUN3D	SA	none	2.00E-04
	2		SA	Venkatakrisnan	2.00E-04
	3		DDES	none	2.00E-04
	4		DDES	Venkatakrisnan	2.00E-04
D	1	EZNSS	SA	unknown	unknown
	2		SST		unknown
	3		TNT		unknown
E	1		SA	unknown	none
	2		SA		1.56E-03
	3		SA		7.81E-04
	4		SA		3.91E-04
F	1	Edge	SA	unknown	1.00E-03
	2	Edge	DDES		1.00E-03
	3	SU2	SA		1.00E-03
	4	Edge	k-omega		1.00E-03
G	1	CFX	SA	BarthJespersion	none
	2	CFX	SA		3.13E-03
	3	CFX	SA		1.56E-03
	4	CFX	SST		none
	5	CFX	SST		3.13E-03
	6	CFX	SST		1.56E-03
	7	CFX	SST		7.81E-04

Table 7. Continued.

Analyst Code	Subcase Number	Software Name	Turbulence Model	Flux Limiter	Time Step (sec)
G, contd	8	FLUENT	SA		none
	9	FLUENT	SA		3.13E-03
	10	FLUENT	SA		1.56E-03
	11	FLUENT	SA		7.81E-04
	12	FLUENT	SST		none
	13	FLUENT	SST		3.13E-03
	14	FLUENT	SST		1.56E-03
	15	FLUENT	SST		7.81E-04
H	1	LOCI/Chem	SA	Venkatakrishnan	none
	2		SA		9.77E-04
	3		SA		2.44E-04
	4		SA		4.88E-04
	5		SST		none
	6		SST		1.00E-03
I	1	OpenFoam	None	GammaDifferencing	none
J	1	ENFLOW	SST	unknown	unknown
	2	ENFLOW	SST	unknown	unknown
	3	(pk method) NASTRAN	None	none	none
K	1	SU2	SA	Venkatakrishnan	none
	2		SA		1.56E-03
	3		SA		7.81E-04
	4		SA		3.91E-04
	5		SA		2.00E-04
	6		SA-COMP		7.81E-04
	7		SA-Edwards		7.81E-04
	8		SST		7.81E-04
	9		SA-comp		2.50E-05
L	1	LAVA	SA	ZWENO5	1.00E-03
	2		DDES	ZWENO5	1.00E-05
	3		DDES	ZWENO5-CENT6	1.00E-05
	4		none	WENO6	none
	5		none	WENO6	2.00E-04
	6		none	WENO6	4.00E-06
M	1	STAR-CCM+	SST	Venkatakrishnan	none
	2		SST		2.40E-04
	3		SST		5.00E-04
N	1	OpenFoam	SA	vanLeer	5.00E-05
O	1	EZAIR	k-w	Vanalbada	1.00E+03
	2		X_LES		1.00E+03
P	1	NSMB	SA	unknown	2.50E-03
	2		k-eps		2.50E-03
	3		k-omega		2.50E-03

**Table 8. AePW-2 Databases.**

Analysis condition	Description	Case Number #	Case Letter Letter	Time accurate solution?	(R)igid or (A)eroelastic	Dynamic pressure (psf)	Database file
Mach 0.7, 3°	Steady rigid	1	a	no	R	N/A	1a
	Forced oscillation	1	b	yes	R	N/A	1b
Mach 0.74, 0°	Steady Rigid	2	a	no	R	N/A	2aR
	Static Aeroelastic at the experimental flutter onset condition	2	a	no	A	169	2aSaeQE
	Static Aeroelastic at the computational flutter onset prediction	2	a	no	A	varies	2aSaeQF
	Dynamic Aeroelastic (flutter solution process) at the experimental flutter onset condition	2	c	yes	A	169	2cQE
	Dynamic Aeroelastic (flutter solution) at the computational flutter onset prediction	2	c	yes	A	varies	2cQF
Mach 0.85, 5°	Steady Rigid	3	a	no	R	N/A	3aR
	Unforced unsteady (time-accurate solution of the rigid unforced case)	3	a	yes	R	N/A	3aU
	Static Aeroelastic at the chosen common analysis condition	3	a	no	A	204	3aSaeQE
	Static Aeroelastic at the computational flutter onset prediction	3	a	no	A	varies	3aSaeQF
	Forced oscillation	3	b	yes	R	N/A	3b
	Dynamic Aeroelastic (flutter solution process) at the chosen common analysis condition	3	c	yes	A	204	3cQE
	Dynamic Aeroelastic (flutter solution ) at the computational flutter onset prediction	3	c	yes	A	varies	3cQF